UNIVERSITY OF CALIFORNIA SAN DIEGO

Light-Mediated Approach for Modeling Dynamic Properties of the Mucin Glycocalyx

A thesis submitted in partial satisfaction of the requirements for the degree

Master of Science

in

Biology

by

Michelle Huiya Zhang

Committee in Charge:

Professor Kamil Godula, Chair
Professor James Wilhelm, Co-Chair
Professor Gulcin Pekkurnaz

2021

The thesis of Michelle Huiya Zhang is approved, and it is acceptable in quality and form for publication on microfilm and electronically.

University of California San Diego

2021

Dedication

I dedicate this thesis to my mom and grandma, who christened me as the pulse of the family—all my feelings and my dreams would be theirs too. Just as they cared for me in my formative years, I dream to be their strength now.

TABLE OF CONTENTS

LIST OF ABBREVIATIONS

CHO: chinese hamster ovary

Chol: cholesterol

CuAAC: copper(I)-catalyzed azide alkyne cycloaddition

DCM: dichloromethane

DIPEA: *N, N*-Diisopropylethylamine

DMF: dimethylformamide

DMSO: dimethylsulfoxide

DP: degree of polymerization

DPPE: 1,2-Dipalmitoyl-sn-glycero-3-phosphorylethanolamine, phospholipid component

DSC: *N,N'*-Disuccinimidyl carbonate

ECM: extracellular matrix

ECA/ECL: *Erythrina cristagalli* agglutinin/lectin

EDC: 1-Ethyl-3-(3-dimethylaminopropyl)carbodiimide

GP: glycopolymer

GPC: gel permeation chromatography

HRMS: high resolution mass spectroscopy

IR: infrared spectroscopy

ECH: epichlorohydrin

pECH: poly(epicholorhydrin)

PEG: polyethylene glycol

p(GA): poly(glycidyl azide)

MsCl: methanesulfonyl chloride

NHS: N-hydroxysuccinimide

NMR: nuclear magnetic resonance

$TBAN_3$: tetrabutylammonium nitride

THF: tetrahydrofuran

TLC: thin layer chromatography

WT: wild type

3D: three dimensional

LIST OF FIGURES

LIST OF APPENDIX FIGURES

ACKNOWLEDGEMENTS

I would like to thank my parents, Yangli Meng and Jianjun Gong, for all of their support for my academic and extracurricular endeavors throughout my life. I attribute my success to them, and I hope I can see them soon.

My PI, Professor Kamil Godula, deserves immense acknowledgment for his generous support and mentoring throughout my research career. He took a chance on me when I was a freshman, and I am very grateful for this opportunity to learn about synthetic chemistry and glycobiology. He consistently provided valuable insight and warm encouragement during this thesis process.

I would like to thank Dr. Daniel Honigfort for all of his time and patience in mentoring me and helping me become the student and scientist I am today. I came into the lab with little experience and Dan taught me everything that I know about synthesis, experimental design, troubleshooting etc. He always took time to answer my questions and guide me on next steps. Dan has been there to support me as a teacher and as a friend, until the very end, so words cannot express how much I appreciate him.

I extend my gratitude to everyone in the Godula Laboratory for all of their kind support and mentorship over the years. In particular, I worked closely with Garland Jackson and Sean Purcell on this project. In addition, Austen Michalak, Bryce Timm, Taryn Lucas, Matt Nattichia, Dr. Ryan Porell and Julianna Follmar have all offered their support and time to help me in the process. I would like to thank Hans Ng for helping me with data collection and choosing to further this project after my departure.

Professor James Wilhelm has been an incredible model during my time working with him as a student and as an instructional assistant. I am very grateful for the support that Professor Wilhelm has provided me during my academic career. I have developed a passion for teaching that I will incorporate into my future career as a doctor.

I would like to thank Professor Gulcin Pekkurnaz for her time and support as my committee member.

ABSTRACT OF THESIS

Light-Mediated Approach for Modeling Dynamic Properties of the Mucin Glycocalyx

By

Michelle Huiya Zhang

Master of Science in Biology

University of California San Diego, 2021

Professor Kamil Godula, Chair
Professor James Wilhelm, Co-Chair

The cell surface glycocalyx is a dense layer of macromolecules of variant structure and size, the latter of which is an underappreciated factor in many cellular functions, such as cell/pathogen interactions, growth factor signaling, cell adhesion/migration, and signal transduction. Methods to alter cellular glycocalyx composition would allow for the study and control of these functions. In the absence of genetic tools to manipulate glycosylation with high spatial specificity, chemical and materials-based approaches offer unique opportunities.

In this study, we developed a transient model for glycocalyx remodeling by photopatterning cells with a novel mucin-mimicking, photocleavable lactose glycopolymer. Subsequently, we applied this model to modify the lectin-binding ability of Lec8 CHO cells, mammalian cells lacking lactosyl residues. Characterization of the lactose glycopolymer, as a free molecule and attached to cells, revealed that photocleavage occurs within 2 minute of UV treatment, confirming the biological utility of this model. Incorporation of lactose glycopolymers into the plasma membrane altered native glycocalyx dynamics and increased lactose-specific lectin, *Erythrina cristagalli* (ECA/ECL), binding at the cell surface. Subsequent cleavage of glycopolymers following UV treatment reduced lectin binding by 80%. These results established this photocleavable glycopolymer as a dynamic model for glycocalyx remodeling and achievement of specific cellular outcomes. In the future, this model can be utilized for biomimicry of events such as mucin shedding during pathogenic invasion and cancer progression.

INTRODUCTION

Chapter 1: The Mucin Glycocalyx

The cellular glycocalyx is a dense layer of heavily glycosylated and highly charged macromolecules, composed of glycoproteins, proteoglycans, and glycolipids (Möckl, 2020). This border of "sweet husk" is the cell's first point of contact with the extracellular matrix and thus mediates all cellular interactions with its environment, ranging from physical protection to communication and signaling (Varki, 2017). Glycans perform these functions primarily through recognition and binding with lectins, or glycan binding proteins (Huang, 2014). The composition and size of these glycoconjugates vary vastly **(Fig 1),** ranging from tens of nanometers above the plasma membrane to thousands of nanometers, as determined by their diverse and often complex glycosylation patterns (Huang, 2016). In general, cellular glycosylation patterns are responsive to the cell-type, developmental stages, and metabolic states of the cell (Hart, 2011).

A major structural constituent of the glycocalyx, cell surface mucins are bulky, abundant, and filamentous glycoproteins that compose the epithelial mucosal lining (Ganguly, 2020). Cell surface mucins mediate interactions between epithelial cells and their environments by preventing entry of unwanted substances and organisms, while mediating endogenous interactions through their elaborate structures **(Fig 1)** (Huang, 2016**)**. Examples of mucin function include trapping invading microbes, acting as decoy receptors via shedding, interacting with immune cells, and sequestering soluble factors (Ganguly, 2020). Due to their special structure and position, mucins play critical roles in many disease processes in which the interactions of epithelial cells and their surroundings are compromised, such as in infectious disease as well as cancer and metastasis (Lindén, 2009; Nath, 2014). Hence, the study of mucin structure and associated functions have important clinical implications. For

example, hyper-sialylation of glycans in tumor-associated mucins (TA-MUC1) causes premature termination of chain elongation (Nath, 2014). Mucins with truncated sugar branches are less stable and more prone to internalization. Inside the cell, these truncated mucins have oncogenic signaling abilities that ultimately contribute to cancer progression and metastasis (Nath, 2014). This makes cell-associated mucins (MUC1) an ideal cancer biomarker and target of cancer immunotherapy (Nath, 2014).

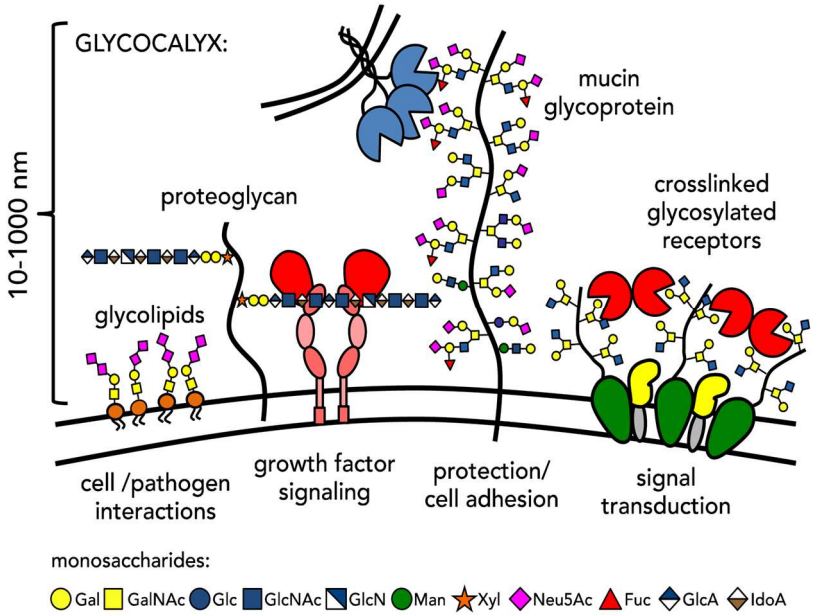

Figure 1 (Huang, 2016): Diversity of the glycocalyx. The cellular glycocalyx is a dynamic, carbohydrate-rich macromolecular system that occupies the boundary between a cell and its surroundings. It is composed of a range of glycolipids and glycoproteins, which can extend tens to hundreds of nanometers above the plasma membrane. The glycocalyx has many functions, ranging from providing cells with a physical protective barrier to facilitating their interactions with their environment. These interactions are primarily mediated through recognition and binding between glycan structures distributed throughout the glycocalyx and the wide array of glycan binding proteins, or lectins.

Chapter 2: Glycocalyx Remodeling and Mucin Mimetics

Glycan contributions in the cell have yet to be fully understood given the complex nature of its biosynthesis, presentation in 3D space, and binding characteristics. In vivo, glycosylation is a post-translational modification carried out in the endoplasmic reticulum (ER) and Golgi apparatus by glycosyltransferases and glycan-processing enzymes (Stanley,

2017). Exploiting different aspects of this biosynthetic pathway, researchers have developed methods and models for elucidating glycan-specific functions and pathways in addition to controlling glycocalyx composition. Examples include targeting gene expression of glycosylation enzymes to attenuate glycan expression and influence glycan assembly; introducing exogenous enzymes to add or cleave specific glycan residues; and supplying modified monosaccharides to the sites of glycosylation to interfere with normal glycan biosynthesis (Esko, 2009; Lopez, 2017; Dube, 2013). These tools result in the global modification of glycan features across entire classes of glycoconjugates, and thus lack control over cell-surface presentation or nanoscale organization (Purcell, 2019).

Nanoscale glycomaterials have been developed to mimic the various components of the glycocalyx and shed light on how glycan presentation (individually and as an ensemble) can influence their biological functions. Among the various approaches, the Bertozzi lab's hydrophobic insertion approach achieves glycocalyx remodeling by functionalizing glycopolymers, chemically synthesized glycoconjugates, with lipid moieties to allow for passive insertion of glycopolymer into the cellular membrane (Mauris, 2013; Paszek, 2014). Utilizing this approach, Honigfort et al. designed synthetic mucin-mimicking glycopolymers to study the physical and steric effects of cell surface mucins on lectin binding abilities with endogenous ligands (2019). Specifically, novel polyethylene glycol (PEG)-based glycopolymers were synthesized with biologically-inert glycans and delivered to the cell surface of turkey red blood cells to mimic the extended architecture of mucin glycoproteins and constitute a "spectator glycocalyx" (Honigfort, 2019). Results suggest altering the physical properties of the glycocalyx resulted in reduced overall lectin binding (Honigfort, 2019). Though providing valuable insight into the physical and mechanical effects of glycocalyx bulk, this model does not allow for dynamic control over glycopolymer patterning of the cell surface, which I aim to do in my research.

Chapter 3: Photocaging: Method for Spatial and Temporal Control

Literature points to light as a dynamic stimulus with many advantages: non-invasive, highly accurate in space and time, and versatile for both 2D and 3D models (Wegner, 2015). Coumarin and ortho-nitrobenzyl cages have emerged as popular strategies for photo-control. Coumarin cages are fluorescent and therefore allow the quantification of photorelease; however, they suffer from unintended photorelease during imaging due to same wavelength for imaging and uncaging (Gaur, 2019). In contrast, ortho-nitrobenzyl cages are incapable of providing quantification unless covalently bound to a fluorescent moiety (Gaur, 2019).

The photocleavable ortho-nitrobenzyl linker has been applied extensively in nano-scale polymer engineering; examples include biofilm engineering and biomimicry of the extracellular matrix (Chen, 2019; Kaneko, 2011; Nicolas, 2020). In these experiments, the nitrobenzyl linker was utilized to pattern functionalized surfaces and scaffolds with bioactive molecules or cells and accomplish specific biochemical outcomes (local release of bioactive molecules or bacterial patterning with high spatial resolution) (Chen, 2019; Kaneko, 2011; Nicolas, 2020; Wegner, 2015).

Furthermore, the photolabile nitrobenzyl linker has been applied to in-vivo models. In a 2019 study, Gaur and Kucherak prepared and tested a set of fluorescent cages that covalently tethers fluorescent rhodamine dyes to signaling lipids via a nitrobenzyl group. This allowed for the delivery of signaling lipids to specific cellular membranes (plasma membrane or inner membrane), with further visualization, quantification, and controlled photorelease of active lipids in living cells (Gaur, 2019). This thesis project utilizes a similar approach to design glycopolymers capable of localization, visualization and biological function.

Chapter 4: Project Overview

This project builds on my previous work constructing the spectator glycocalyx by adding a photocleavable component to the glycopolymer design (Honigfort, 2019; Kaneko, 2011). A novel photocleavable glycopolymer was created to dynamically remodel the mucin glycocalyx in mammalian cells **(Fig 2)**. To do this, first, I prepared and characterized the photocleavable glycopolymer (**Fig 2A**). A PEG polymer backbone was end-functionalized with the nitrobenzyl linker, connected on the other end to a lipid moiety (Honigfort, 2019; Kaneko, 2011) (**Fig 2A**). Then the PEG backbone was sidechain-functionalized with lactose and Cy5 fluorophore (Honigfort, 2019) (**Fig 2A**). Second, I delivered these novel glycopolymers to the cell surface of CHO Lec8 cells, a mutant strain with endogenous lactose synthesis disrupted, to alter their native glycocalyx and restore lactose-specific ECA (*Erythrina Cristagalli*) lectin binding (**Fig 2B and C**). Subsequently, I optimized conditions for photocleavage and significantly reduced ECA binding levels through removal of glycopolymers from the cell surface (**Fig 2B and C**). This model will be a useful tool in creating biomimicry systems for cellular events involving mucins, such as endogenous mucin shedding after pathogen detection and trapping (Lindén, 2009).

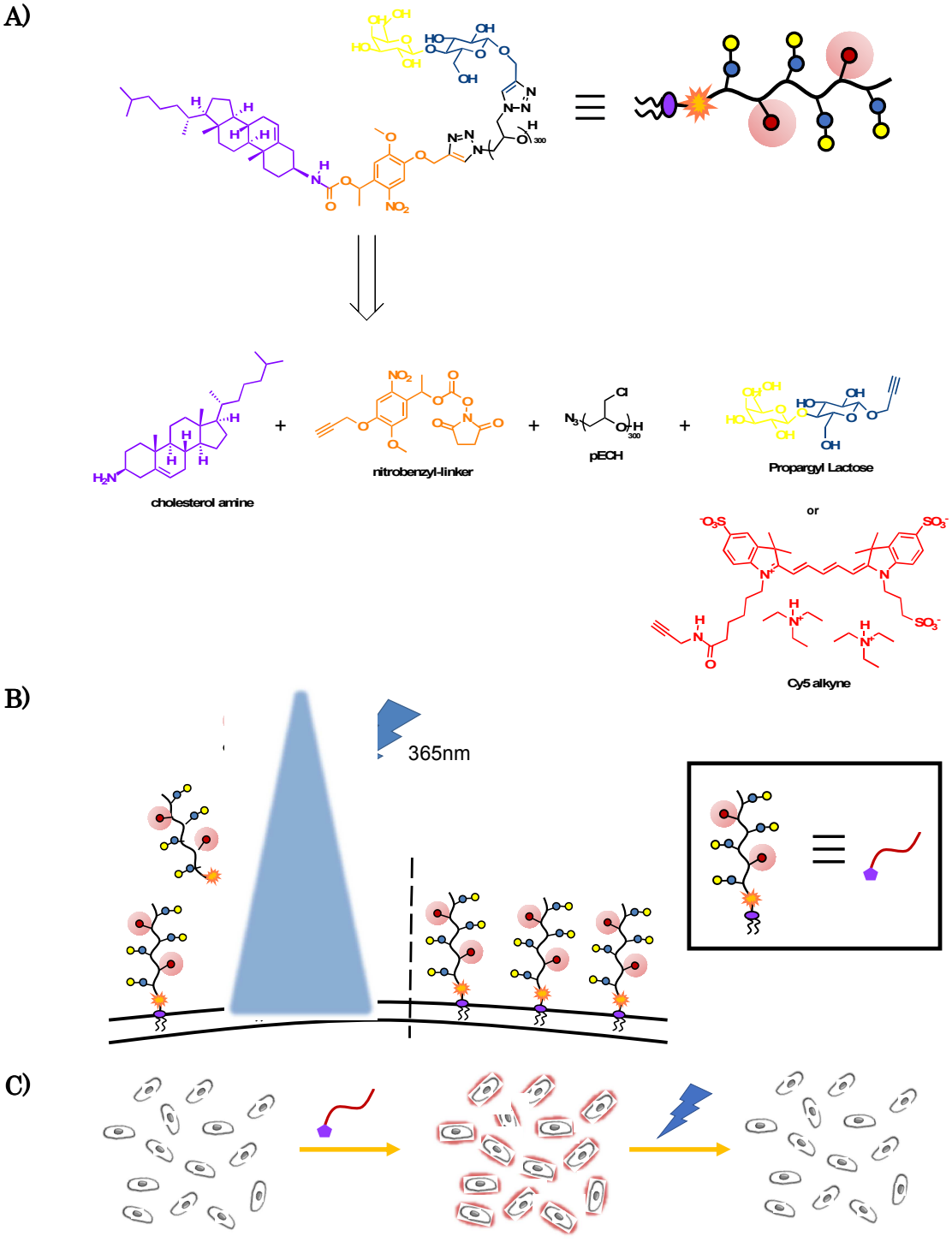

Figure 2: Light-mediated remodeling of the mucin glycocalyx. A) Retrosynthetic scheme of photocleavable glycopolymer. B) Photopatterning cell surfaces with photolabile synthetic glycopolymers allows spatial and temporal control over glycocalyx engineering. C) This method of photopatterning and subsequent photocleavage at 365nm is applied to mammalian cells in suspension.

EXPERIMENTAL RESULTS

The goal of developing a new method to dynamically change the physical and biological properties of the glycocalyx using light as a stimulus is achieved in 3 steps:

1. Synthesize glycopolymers with or without photocleavable properties
2. Photopattern cell surface with synthetic glycopolymers to achieve spatial and temporal control over the glycocalyx
3. Study the effects of photopatterning on lectin binding abilities of the cell

Aim 1: Creating Photocleavable and Control Mucin Mimetics

This study was initiated by establishing a synthetic strategy to generate glycopolymer structures that can be introduced to the cell surface and removed upon external stimulus. The general glycopolymer design was adapted from Honigfort, 2019, which detailed an azide terminated poly(epichlorohydrin) p(ECH) backbone that was subsequently functionalized with propargyl glycosides and fluorophore-alkyne. The azide endgroup on the polymer backbone allowed attachment of alkylated linkers and lipid moieties through copper-click chemistry (copper-catalysed alkyne-azide cycloaddition CuAAC). The photolabile component was introduced through the ortho-nitrobenzyl linker, which was also adapted from literature (Wegner, 2015; Kaneko, 2011). One end of the linker contained an alkyne (for attachment to the azide terminal p(ECH)), and the other end was functionalized with a NHS group, as NHS-amine chemistry is also highly efficient. The NHS group allowed for the attachment of the lipid moiety for specific targeting of the plasma membrane. This section details the synthesis and characterization of components and finished products of the photocleavable and control glycopolymers.

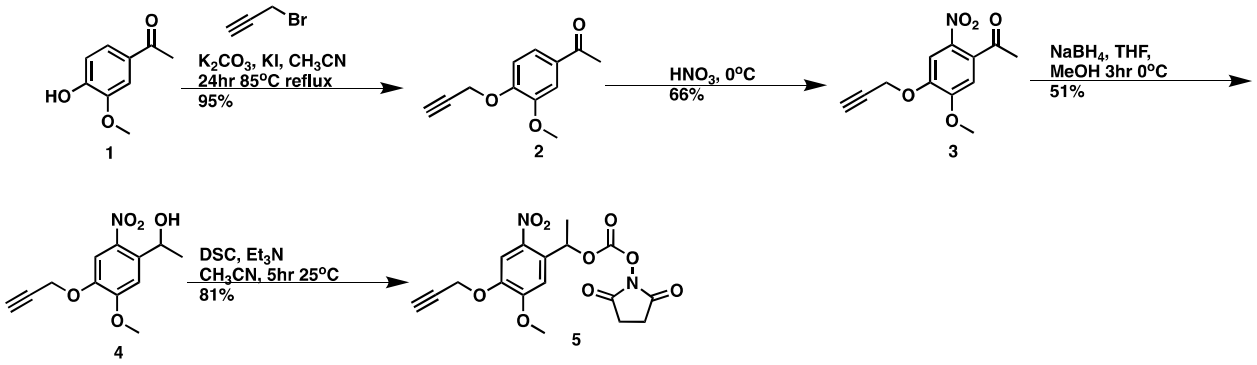

Figure 3: Synthesis of photocleavable bifunctional linker.

The photocleavable nitrobenzyl linker **5** was synthesized in four steps (**Fig 3**). First, commercially available acetovanillone **1** was alkylated with propargyl bromide under basic conditions to yield compound **2** (Kaneko, 2011). Then, nitration of the aromatic ring using nitric acid at 0°C yielded the nitrated compound **3** (Govan, 2013). Third, reduction of the ketone using sodium borohydridxe yielded the secondary alcohol **4** in good yield (Kaneko, 2011). Lastly, conversion of the alcohol to the NHS ester using *N,N'*-disuccinimidyl carbonate (DSC) provided the final bifunctional photocleavable linker **5** (Kaneko, 2011).

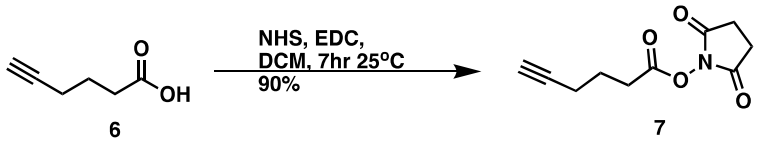

Fig 4: Synthesis of nonphotocleavable bifunctional linker.

In order to ensure that I was measuring cleavage of the photocleavable group and not photobleaching of the fluorophores during UV treatment, I also synthesized a parallel non-photocleavable linker to act as a control. Commercially available 5' hexynoic acid **6** was conjugated with NHS with the help of carboxyl activator EDC to yield the nonphotocleavable bifunctional linker **7** (**Fig 4**).

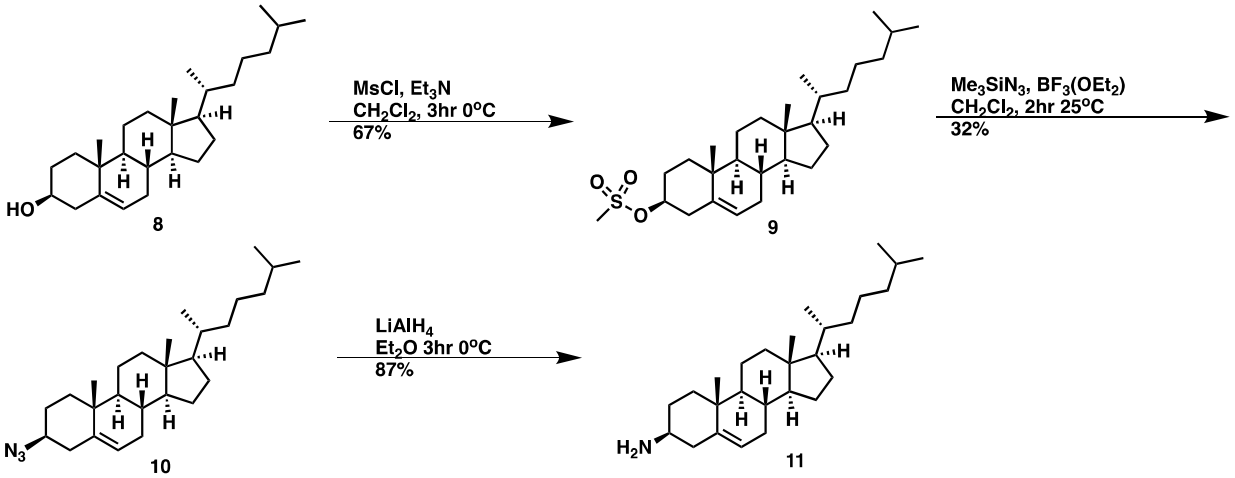

Fig 5: Synthesis of cholesterol-amine hydrophobic endgroup.

In order to incorporate the final glycopolymer onto the cellular membrane, I chose a cholesterol type hydrophobic moiety to serve as the endgroup. Cholesterol and its derivatives have been shown to efficiently incorporate into lipid bilayers (Honigfort, 2019). To couple a cholesterol type molecule to the photocleavable linker using the available NHS chemistry, I converted commercially available cholesterol **8** into a cholesterol-amine by first activating the alcohol as a mesylate **9** (**Fig 5;** Isabettini, 2017). Reaction with an azide source in the presence of $BF_3(OEt_2)$ yielded the azide moiety **10**, which can be reduced to the secondary amine using strong reducing conditions ($LiAlH_4$) to yield cholesterol-amine **11** (Isabettini, 2017).

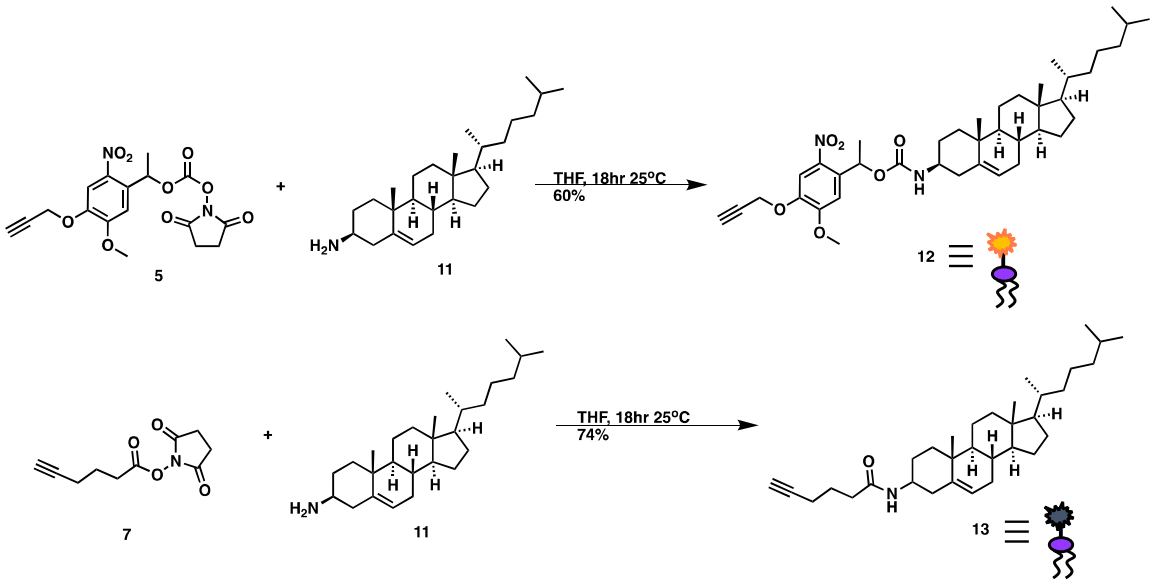

Figure 6: Synthesis of endgroup moieties.

The bifunctional linkers **5** and **7** are each conjugated with cholesterol-amine **11** through NHS-amine coupling before attachment to the polymer backbone (**Fig 6**). These two conjugation reactions yield the photocleavable Chol-Photo endgroup **12** and nonphotocleavable Chol endgroup **13**.

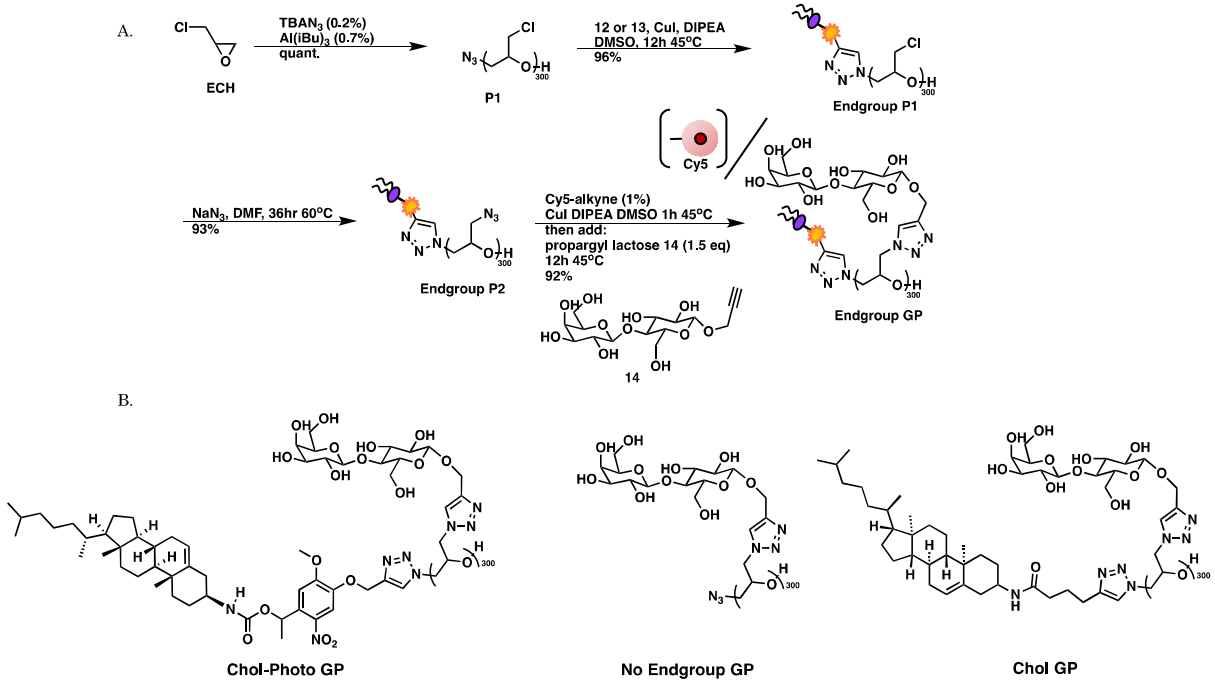

Figure 7: Synthesis and characterization of glycopolymers. A.) synthesis of glycopolymer. B.) structures of final GP.

With all the components in hand, I assembled the glycopolymer according to the protocol detailed in Honigfort, 2019. Using monomer-activated anionic ring opening polymerization, I synthesized an azide-terminated poly(epichlorohydrin) (pECH) polymer **P1** (**Fig 7**) with well-defined size (Mn = 27,700 Da, DP ~300) and narrow chain-length distribution (Đ = 1.23) (Gervais, 2009). The polymer backbone **P1** was subsequently elaborated into fluorescent, cell surface-targeting, photolabile mucin mimetics in a three-step synthetic sequence (**Fig 7**) (Honigfort, 2019). First, I functionalized **P1** with either lipid-linker endgroup **12** or **13** via CuAAC between the chain-end azide group in **P1** and the alkynyl group on the linker (10.0 equiv. per chain-end azide) to yield endgroup-modified pECH polymer **Endgroup P1**. To ensure that the polymer fluorescence detected on the cell surface was due to hydrophobic insertion of the lipid tail and not association between the polymer backbone and the cell surface, I also included a no endgroup glycopolymer control that received the same treatment in this sequence, including step 1. Then, the chloromethyl sidechains in **Endgroup P1** were converted to azidomethyl sidechains through treatment with sodium azide (2.0 eq per Cl) to generate a reactive polymer intermediate **Endgroup P2**. The azide functionalized sidechains allowed for the sequential CuAAC conjugation of alkynyl fluorophores (Cy5, ~ 0.2 % sidechains) and propargyl lactosides **14**, synthesized according to Honigfort et al., to complete the desired glycopolymers **Endgroup GP** (**Fig 7**) (Honigfort, 2019).

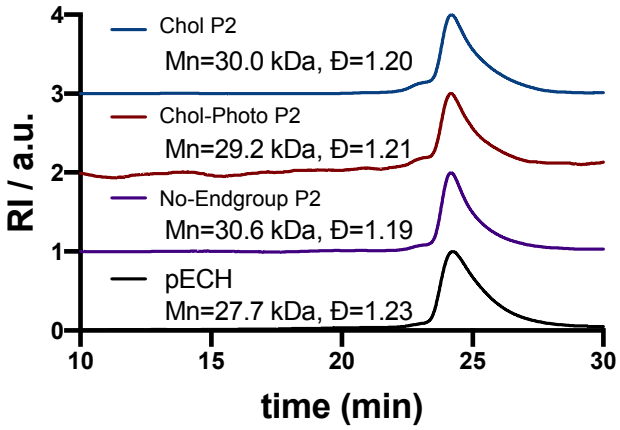

Figure 8: GPC traces of **P1** and **Endgroup P2** show retention of Mn and dispersity (Đ).

GPC analysis of the parent polymer **P1** was compared to the final GP precursor **Endgroup P2** (**Fig 8**). Retention of Mn (Mn = 27-31kDa) and Đ (Đ = 1.19-1.23) indicated that the endgroup CuAAC conjugation and azidation reactions did not significantly degrade the backbone.

1H-NMR spectroscopy analysis of polymeric intermediate **Endgroup P2** confirmed quantitative azide-chloride replacement (**Appendix Fig A22 and A28**). The efficiency of the other steps in the glycopolymer synthesis sequence was difficult to establish accurately based on 1H-NMR spectroscopy alone. The endgroup and polymer conjugation step was difficult to visualize because the proton signals from the backbone significantly overwhelms the endgroup signals (300 repeating units * 5 protons per unit = 1,500 polymer protons per endgroup). In addition, the propargyl-lactoside **14** conjugation to the polymer was difficult to quantify due to the overlap between glycan and polymer proton signals (Honigfort, 2019). IR spectroscopy analysis of glycopolymers was a useful alternative, as the presence and disappearance of the characteristic azide stretching absorption frequency at 2100 cm^{-1}, indicated in red (**Fig 9-11**), is a robust measurement of azide endgroup and side-chain modification (Honigfort, 2019).

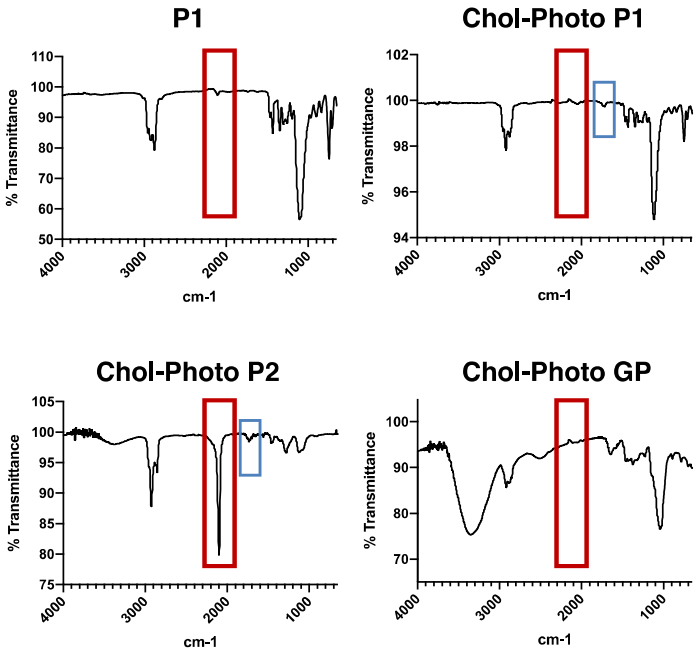

Figure 9: Characterization of **Chol-photo GP** and its synthetic precursors by IR spectroscopy.

IR analysis of **P1** revealed a weak azide signal at 2100 cm^{-1}, which was expected as the azide to sidechain ratio was 1:300 (**Fig 9**). After conjugation of the cholesterol-nitrobenzyl endgroup to the azide-terminated pECH backbone, the azide signal disappeared in **Chol-Photo P1**, confirming success of attachment (**Fig 9**). After converting chloromethyl sidechains to azidomethyl groups, the azide peak drastically increased, as expected (**Fig 9**). Finally, the complete disappearance of the 2100 cm^{-1} stretch in **Chol-Photo GP** indicated quantitative side-chain modification with propargyl lactoside (**Fig 9**). In addition to the azide stretch, the linker attachment contained a carbamate group that displayed the characteristic C=O stretch at 1700 cm^{-1} and was visible in **Chol-Photo P1** and **P2** (**Fig 9**).

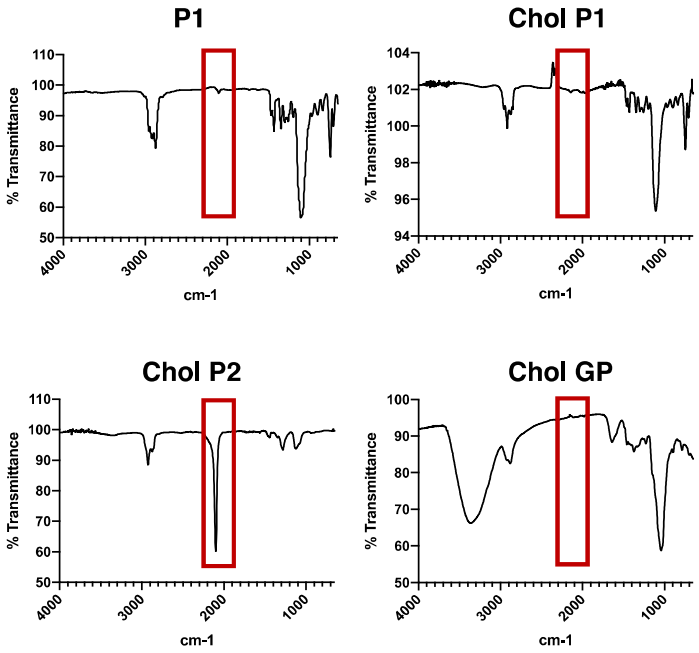

Figure 10: Characterization of **Chol GP** and its synthetic precursors by IR spectroscopy.

In contrast, after conjugation of the cholesterol-hexynoic acid endgroup to the azide-terminated pECH backbone, the azide signal did not disappeared completely in **Chol P1**, suggesting that some polymers did not acquire a lipid tail (**Fig 10**). This may affect downstream experiments, as some polymers would not be able to incorporate into the plasma membrane, so **Chol GP** fluorophore signal after incorporation into cellular membranes was expected to be lower. After converting chloromethyl sidechains to azidomethyl groups, the azide peak drastically increased, as expected. Finally, the complete disappearance of the 2100 cm^{-1} stretch in **Chol GP** indicated quantitative side-chain modification with propargyl lactoside **14** (**Fig 10**).

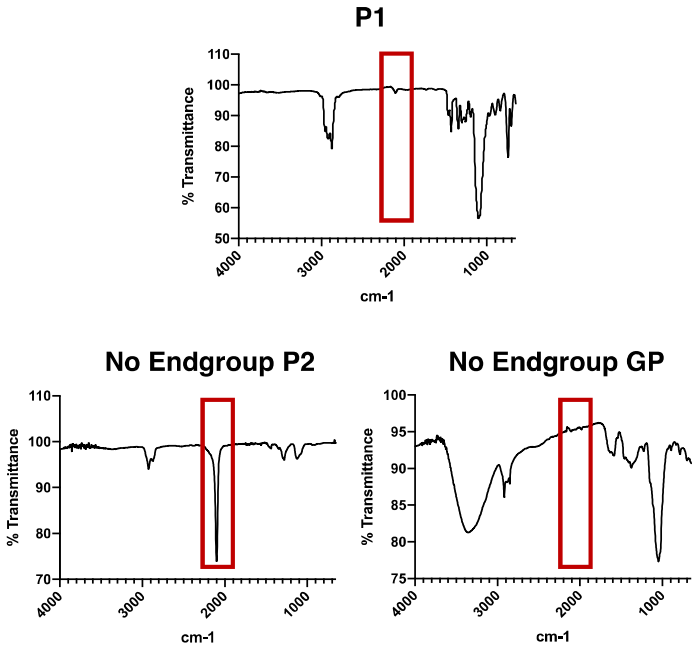

Figure 11: Characterization of **No Endgroup GP** and its synthetic precursors by IR spectroscopy.

The **No Endgroup GP** synthesis sequence displayed the same patterns in IR spectroscopy. Conversion of chloromethyl sidechains to azidomethyl groups saw the azide peak drastically increase and quantitative side-chain modification with propargyl lactoside **14** saw the complete disappearance of the 2100 cm^{-1} stretch (**Fig 11**).

Polymer Condition	Conc.(FL/P)
Chol-Photo GP	0.7998
Chol GP	0.615
No Endgroup GP	0.9294

Figure 12: UV-Vis characterization of glycopolymer labeling with Cy5.

The levels of fluorophore labelling in glycopolymers **Endgroup GP** were assessed based on UV-VIS absorption profiles and matched values predicted based on reaction stoichiometry (**Fig 12**).

A

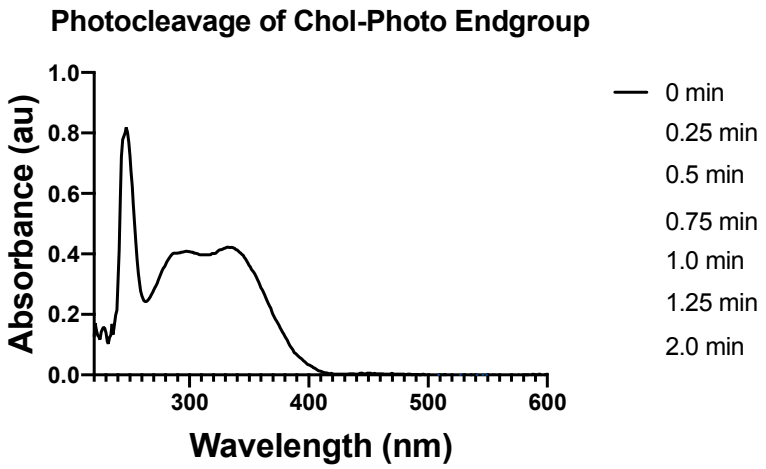

B

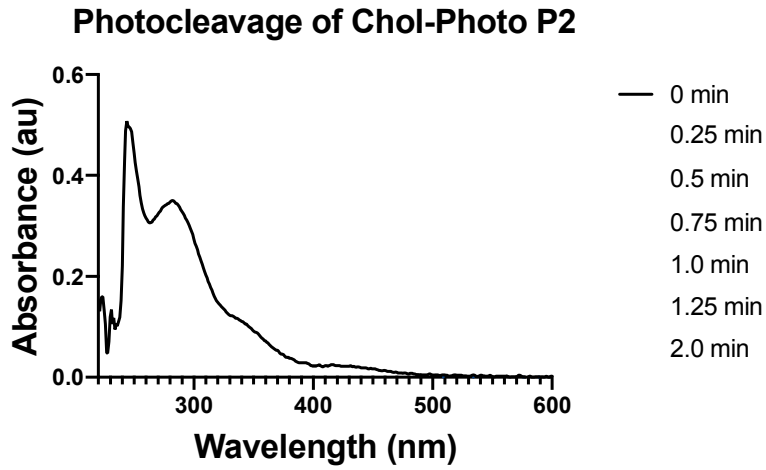

C

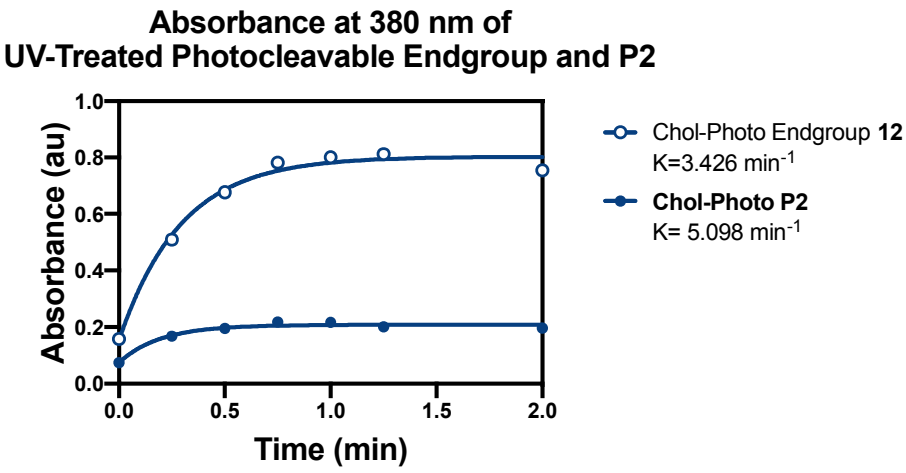

Figure 13: UV-Vis characterization of photocleavage of photocleavable linker **12** and photocleavable glycopolymer **Chol-Photo P2**. A) UV/Vis spectra of photocleavable linker **12** at different time points for UV exposure. B) UV/Vis spectra of photocleavable glycopolymer **Chol-Photo P2** at different time points for UV exposure. C) Absorbance of **12** and **Chol-Photo P2** at 380nm during photocleavage with 365nm light.

To confirm and quantify the photocleavage ability of the cholesterol-nitrobenzyl linker, small molecule **12** and polymer-conjugated **Chol-Photo P2** were dissolved in chloroform and detected on the UV-Vis spectrometer (**Fig 13A and B**). The absorbance peak at 247nm, present in both absorbance curves, was utilized for normalization as this was deemed independent of the photocleavable moieties (**Fig 13A and B**). In the absorbance curve of **12**, the lower absorbance peaks at 297nm and 332nm were characteristic of the intact molecule, as they were only present at time point 0 min (without UV treatment) (**Fig 13A**). When attached to the pGA polymer, the pre-cleavage linker peaks (287nm and 345nm) become shifted and less pronounced, as the UV signals from the polymer attenuated the linker signals. After pre-cleavage characterization at 0s, the molecules were exposed to UV radiation (365nm) and a time course was taken in 0.25 minute intervals (**Fig 13B**). For **12**, the 297nm peak shifted to 267nm, while the 332nm peak shifted to 370nm (**Fig 13A**). Similarly, for **Chol-Photo P2**, the 287 nm peak shifted to 271 nm, while the 345nm peak shifted to 384nm (**Fig 13B**).

To quantify the rate of cleavage, the absorbance data were normalized to the 247nm peak, and absorbance at 380nm for **12** and **Chol-Photo P2** served as an indicator of cleavage progress, since it increased with photocleavage time (**Fig 13C**). Monitoring the absorbance at 380nm and fitting to a best fit curve allowed for determination of cleavage rate in chloroform. The rate of photocleavage for the cholesterol-nitrobenzyl linker **12** was quantified from the linear regression as 3.426 min^{-1}, and photocleavage was complete by 1.0 minute (**Fig 13A and C**). Similarly, the rate of photocleavage for the cholesterol-nitrobenzyl functionalized p(GA) polymer **Chol-Photo P2** was quantified as 5.098 min^{-1}, and photocleavage was complete by 0.75 minute (**Fig 13B and C**). The photocleavage rate of the linker seemed consistent between small molecule and attached to polymer. Comprehensively, UV-spectroscopy data validated

the photocleavage ability of **12** and **Chol-Photo P2**, and quantified the rate of photocleavage, thus capacitating the next step of the project: photopatterning of cellular plasma membranes.

Aim 2: Creating Dynamic Light-Mediated Model for Glycan Presentation

Now that I have generated these glycopolymers, I sought to apply them to cell surfaces to establish a controllable glycocalyx. To establish this dynamic light-mediated model of glycocalyx remodeling, I developed methods to localize the photocleavable glycopolyemer **Chol-Photo GP** to the plasma membrane and subsequently remove it upon external activation. These cellular modifications were tested with flow cytometry. Mammalian CHO Lec8 cells were selected for this study because its specifications: lacking terminal galactose residues due to a defective UDP-galactose transporter into the Golgi, were important for the downstream lectin binding assays (Stanley, 1989).

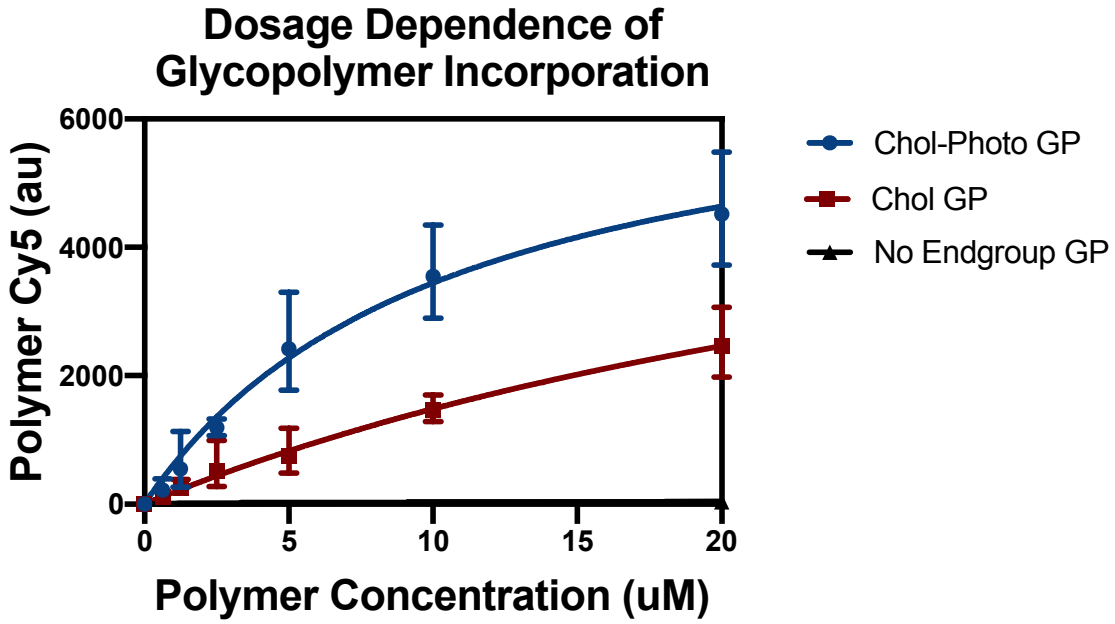

Figure 14: Incorporation of glycopolymers into the plasma membrane of CHO Lec8 cells is dosage dependent.

CHO Lec8 cells were incubated with increasing concentrations of glycopolymer (0.625 μM - 20 μM) for 60 minutes at 0 °C. Incubation at 0 °C effectively reduced glycopolymer internalization. Samples were kept on ice in subsequent steps as well. After incubation, the cells were washed 3X and resuspended thoroughly before running on the flow cytometer to quantify cell surface Cy5 fluorescence. As the concentration of glycopolymer increases, more gets incorporated. The trend was not strictly linear, indicating that there is a point of saturation, as others have observed (**Fig 14**) (Honigfort, 2019). Fluorescence signal began to plateau at 10 μM, so 5 μM was chosen as polymer incubation concentration in all future experiments as it was the last point of the linear phase on the incorporation curve (**Fig 14**). The **No Engroup GP** was synthesized and tested as an incorporation control to confirm that glycopolymers without a cholesterol could not incorporate (**Fig 14**). Results confirmed that incorporation of polymers was lipid endgroup-dependent. **Chol-Photo GP** incorporated at a slightly higher rate than the **Chol GP**, potentially due to the presence of an additional aromatic ring that extended the hydrophobic domain or the incomplete lipidation of polymer endgroup azide in **Chol GP** (**Fig 10**).

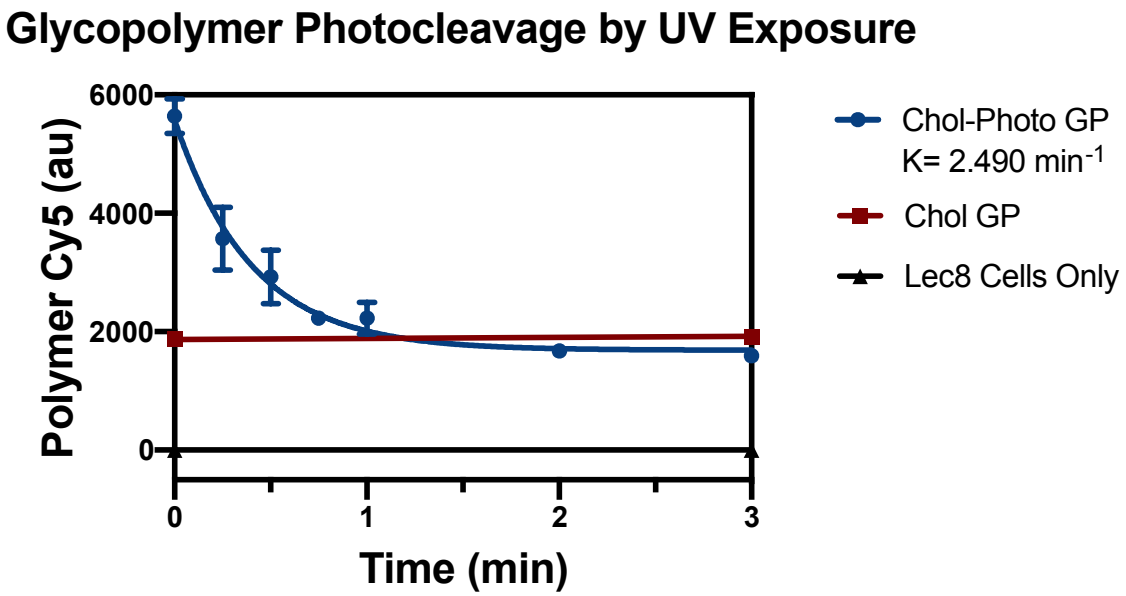

Figure 15: Photocleavage of glycopolymers from the plasma membrane of CHO Lec8 cells is complete by two minutes.

Then, I tested the photocleavage of the glycopolymers as a function of time (**Fig 15**). CHO Lec8 cells were incubated with 5 μM glycopolymer, washed 1X, and UV treated with a 15-Watt UV source for increasing amounts of time (0.25 minute – 2 minutes). These samples were then run on the flow cytometer to quantify cell surface Cy5 fluorescence with and without UV treatment. In this case, reduction of Cy5 fluorescence was used as a direct measure of photocleavage. Nonphotocleavable polymer **Chol GP** was included as a control, which did not reduce fluorescence signal with UV exposure, confirming that the loss of fluorescence in the experimental condition was indeed due to removal of glycopolymers from the cell surface via photocleavage (**Fig 15**). The rate of photocleavage for **Chol-Photo GP** was quantified from the one-phase decay curve to equal 2.490 cm^{-1}, and photocleavage was complete by 2 minutes (**Fig 15**). This rate was similar but slower compared to that of the small molecule **12** and the non-glycosylated **Chol-Photo P1.** Many factors may have contributed to this. For example, the nitrobenzyl linker may be less accessible after

glycosylation and being localized on the cell surface. In addition, the photocleavage from the cell surface was done in water instead of chloroform. Water may disperse light more, affecting the photocleavage and the fluorescence detection. The **Chol-Photo GP** was reduced by 71.8% when photocleavage was completed at approximately 2 min, as additional UV exposure did not continue to reduce fluorescence signal (**Fig 15**). The overall reduction level and photocleavage rate may be a function of UV treatment setup, so better apparatus to minimize the distance and barriers between the light source and cells may improve these outcomes. Another way to quantify photocleavage and removal of polymer from the cell surface was via lectin staining, which was the focus of Aim 3.

Aim 3: Utilizing Light-Mediated Glycocalyx Engineering Model to Achieve Biological Outcomes

With the ability to dynamically control the presence of glycopolymers on the cell surface in hand, I set about applying the model to lectin binding. Endogenous lectins interact transiently with the glycocalyx and enable the glycans to enact downstream functions. Hence, the ability to control lectin binding at the cell surface via control over glycan presentation has important biological implications and applications. As mentioned before, mammalian CHO Lec8 was selected for this study because its specifications were important for the lectin binding assays. Lec8 cells have their endogenous galactosyl transporter disrupted, so UDP-galactose is not transported into the Golgi for glycosylation (Stanley, 1989). Without terminal galactose, Lec8 cells have a low background for lactose-specific lectin ECA binding (**Fig 16-18**). By remodeling with photocleavable lactosyl glycopolymers, I aimed to restore and subsequently remove lactose glycans from the Lec8 glycocalyx via UV cleavage.

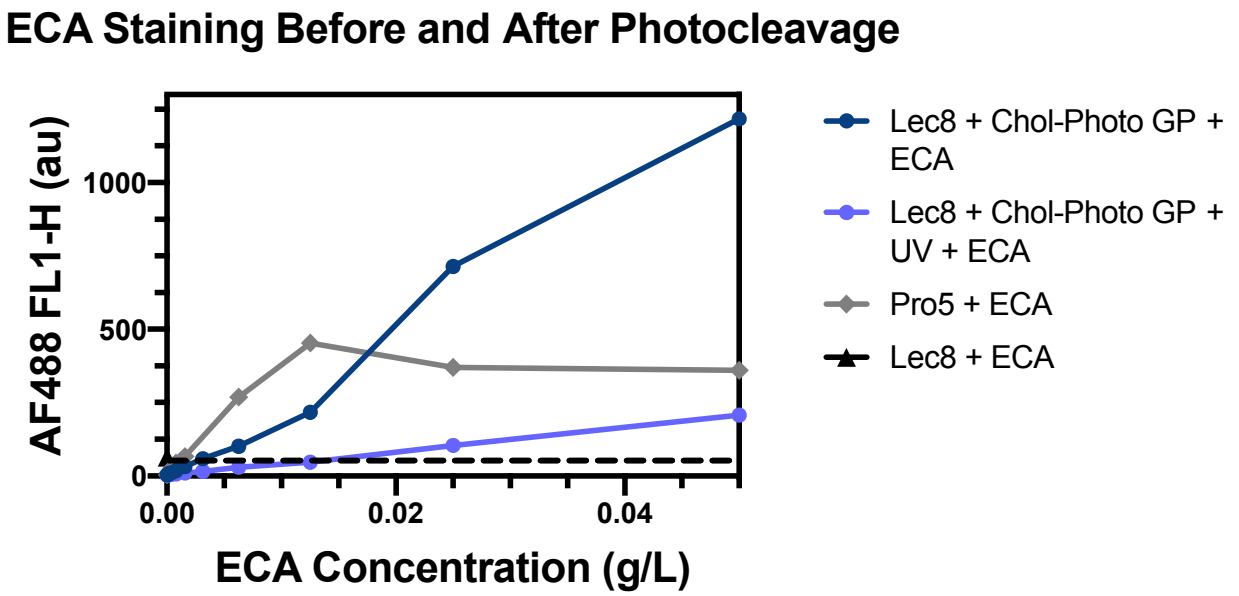

Figure 16: Dosage dependent ECA staining before and after UV treatment (2 min at 365 nm) to optimize lectin concentration. AF488 FL1-H measures fluorescein-labeled ECA signal. Each data point represents a single sample.

Fluorescein-labeled ECA was used to target Cy5-labeled lactosyl glycopolymers and enable two-color visualization via flow cytometry. However, the concentration of lectin needed to be determined empirically. Lec8 cells-only was included as a negative control to test non-specific ECA binding to Lec8 and establish background (**Fig 16**). Pro5 cells, which are CHO wildtype cells, were included as a positive control (**Fig 16**). The experimental conditions had **Chol-Photo GP**-remodeled Lec8 cells UV treated for either 0 minutes or 2 minutes (**Fig 16**). Each condition was then aliquoted into 8 samples, and each sample was incubated with increasing concentrations of fluorescein-ECA (c_{ECA} = 0 - 0.05g/L). The optimal lectin concentration would maximize the difference between UV-treated and non-UV treated experimental conditions without inducing agglutination. Agglutination occurs when multiple cells get crosslinked by the multivalent lectins at high lectin and cell concentrations. It can be detected on the flow cytometer: collected events would display a shift in forward and side scatter, and the events per second would drastically reduce since aggregates of cells were now counted as singular events. The Lec8 cells-only and photocleaved remodeled Lec8 cells did

not reach the agglutination concentration. This was expected, as less lactose residues for lectin binding would increase the threshold agglutination concentration. Pro5 cells agglutinated at 0.0125g/L, 0.025g/L and 0.05 g/L; nonphotocleaved remodeled Lec8 cells agglutinated at 0.025g/L and 0.05 g/L. Pro5 agglutinated at lower ECA conditions, likely due to WT CHO cells having more galactose residues compared to remodeled Lec8 cells. The optimal lectin concentration was determined to be 0.0125g/L, because at that concentration the difference between the photocleaved and nonphotocleaved experimental conditions were maximized without cells agglutinating (**Fig 16**).

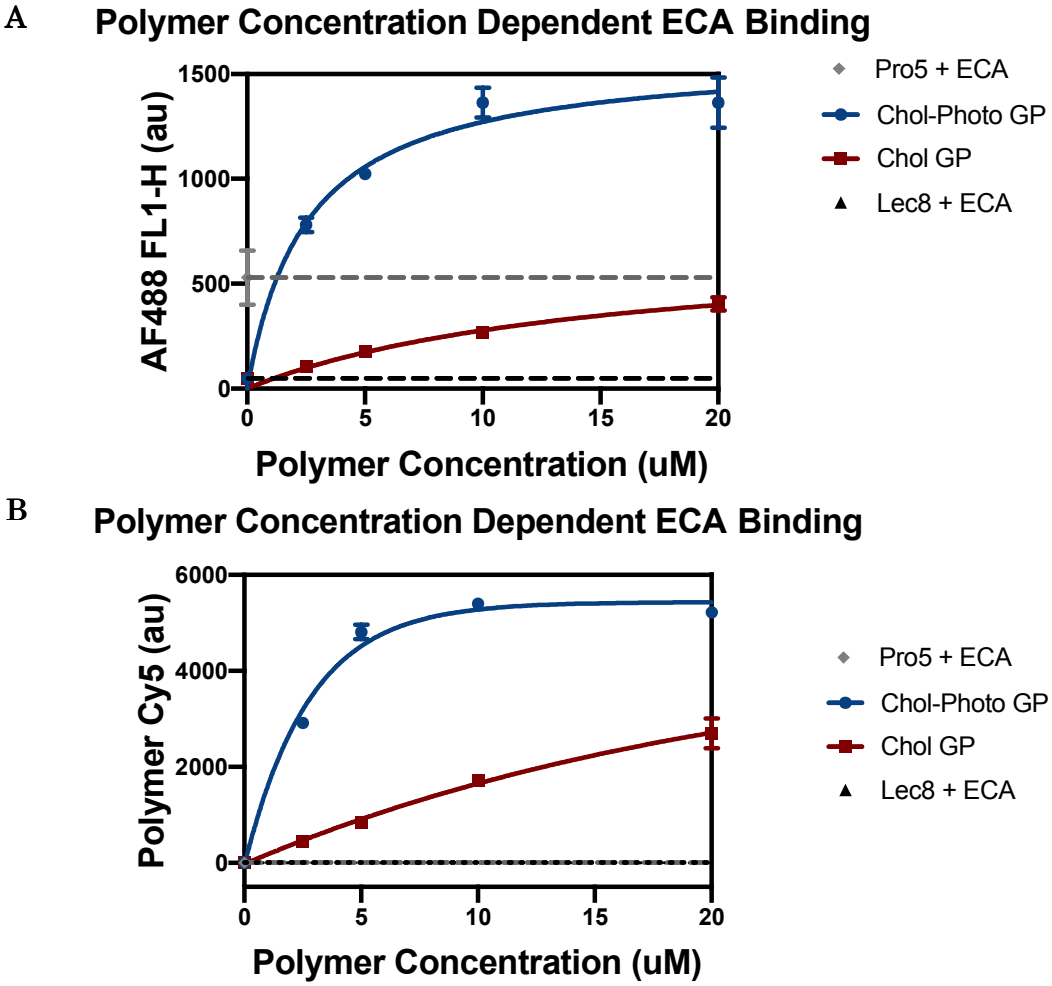

Figure 17: Concentration of lectin ECA binding to the remodeled CHO Lec8 cells is dependent on glycopolymer concentration.

At this point, I have established the optimal conditions for the key components of light-mediated glycocalyx engineering model: 5 μM glycopolymer for incorporation, 2-minute UV treatment for photocleavage, and 0.0125 g/L ECA for lectin staining. With the model established, I set about testing the various characteristics of this model. As an extension of the glycopolymer incorporation experiment in Aim 2, I tested lectin binding efficiency as a function of glycopolymer concentration (c_p=0 μM – 20 μM) (**Fig 17**). Increasing polymer concentration increased lectin binding, as would be expected for binding to incorporated lactose residues. The trends of the fluorescein-ECA signal (**Fig 17A**) were congruent with that of the Cy5-glycopolymer signal (**Fig 17B**) as polymer concentration increased.

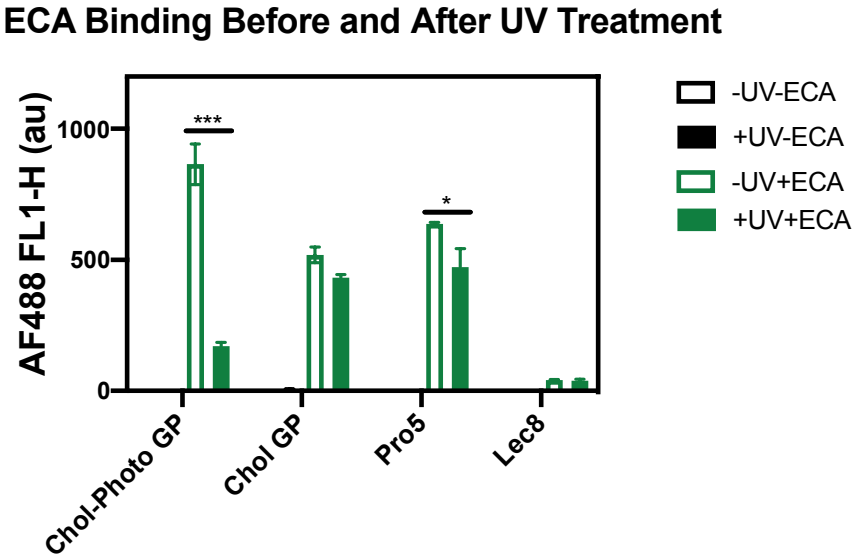

Figure 18: Lectin ECA binding to CHO Lec8 cells is restored following glycopolymer incorporation and subsequently reduced following photocleavage. Lec8 cells remodeled at 5μM polymer concentration. ANOVA, Tukey's multiple comparisons test; p*<0.05; p*** < 0.001.

Lastly, I tested the efficiency of ECA binding before and after UV treatment of photocleavable and nonphotocleavable glycopolymers (**Chol-Photo GP** and **Chol GP, respectively**) with the established parameters. Data analysis suggested that ECA binding was

significantly reduced (80.3%) following photocleavage for the **Chol-Photo GP** remodeled Lec8 cells (**Fig 18**). The other groups served as controls and did not exhibit significant change. There also seemed to be significant reduction in lectin signal following UV treatment in the Pro5 cells, however the p value was 0.045, so the significance of this result was ambiguous and may be due to varying levels of agglutination between the samples (**Fig 18**). Overall, these results confirmed that this mucin-glycocalyx engineering method is successful in delivering lactosyl mucin mimetics to the cell surface and removing these glycopolymers, with downstream lectin-binding effects, establishing temporal control over cell surface glycosylation.

DISCUSSION AND FUTURE DIRECTIONS

In this study, I developed a transient model for glycocalyx remodeling by photopatterning cells with a novel mucin-mimicking, photocleavable glycopolymer; subsequently, this model was applied to modify the lectin-binding abilities of CHO Lec8 cells. The novel glycopolymer was end-functionalized with a photocleavable nitrobenzyl linker, linking the backbone to a cholesterol moiety for membrane incorporation, and sidechain-functionalized with lactosides and Cy5 fluorophore (for visualization). Using this non-covalent cell membrane engineering approach, I introduced these lactosyl glycopolymers to the cell surface of CHO Lec8 cells, a mutant strain unable to express lactose residues in the glycocalyx. Incorporation of lactosyl glycopolymers into the plasma membrane increased lactose-specific ECA-fluorescein signal at the cell surface; subsequent cleavage of glycopolymers following UV treatment significantly reduced lectin fluorescence. Characterization of photocleavage suggested that cleavage completed within 2 min of UV treatment. This short, biologically relevant timescale for glycocalyx remodeling renders this model suitable for mimicking cellular events related to the glycocalyx.

The next step is to optimize the same biological experiments (glycopolymer incorporation, photocleavage, and lectin staining) in adherent cells and examine with microscopy. As a spatially and temporally controlled glycocalyx remodeling method, it is essential that these findings are applicable to adherent cell models as well. I have conducted and collected data from preliminary microscopy experiments, but they are not optimized to publication quality.

Once developed, this model can be utilized for studying biological mechanisms involving cell-surface mucins. For example, bacterial and viral invaders interact intimately

with cell surface mucins during infection. Mucins are often shed as decoys to physically trap and remove pathogenic invaders; however, this process forms holes in the glycocalyx to expose the underlying host cell, making it more susceptible to infection (Lindén, 2009). In another example, bulky glycoproteins in the glycocalyx interact with cell surface adhesion molecules, such as integrin (Paszeck, 2014). Bulky mucins reduce overall integrin-binding rate but enhance integrin clustering and focal adhesion assembly, which in turn promotes cell growth and survival on highly compliant, usually non-viable surfaces, as in cancer metastasis (Paszeck, 2014). The light-mediated mucin-glycocalyx remodeling method developed in this study would be ideal to study both of these interesting processes.

MATERIALS AND METHODS

Materials. All chemicals, unless stated otherwise, were purchased from Sigma Aldrich and used as received. Reaction progress was checked by analytical thin-layer chromatography (TLC, Merck silica gel 60 F-254 plates) monitored either with UV illumination, or by staining with CAM, ninhydrin, or $KMnO_4$ stain. CHO Lec8 and Pro5 cells used were propagations from cells obtained from ATCC (# CRL-1737 and CRL-1781). Fluorescein-labeled *Erythrina cristagalli* agglutinin/lectin (ECA/ECL) lectin was purchased from Vector Labs. Cyanine 5 (Cy5)-alkyne for labeling of polymers was obtained from Sigma Aldrich.

Instruments. Column chromatography was performed on a Biotage Isolera One automated flash chromatography system. Nuclear magnetic resonance (NMR) spectra were collected on a Bruker 300 MHz and a Jeol 500 MHz NMR spectrometers. Spectra were recorded in $CDCl_3$, MeOD or D_2O solutions at 293K and are reported in parts per million (ppm) on the δ scale relative to the residual solvent as an internal standard (for ^1H NMR: $CDCl_3$ = 7.26 ppm, CD_3OD = 3.31 ppm, D2O = 4.79 ppm, for ^{13}C NMR: $CDCl_3$ = 77.0 ppm, CD_3OD = 49.0 ppm). HRMS (high-resolution mass spectrometry) analysis was performed on an Agilent 6230 ESI-TOFMS in positive ion mode. UV-Vis spectra were collected with a quartz cuvette using a Thermo Scientific Nanodrop2000c spectrophotometer. IR spectroscopy was performed on a Nicolet 6700 FT-IR spectrophotometer (Thermo Scientific). Size exclusion chromatography (SEC) was performed on a Hitachi Chromaster system equipped with an RI detector and two 5 μm, mixed bed, 7.8 mm I.D. x 30 cm TSKgel columns in series (Tosoh Bioscience). Organic soluble polymers were analyzed using an isocratic method with a flow rate of 0.7 mL/min in DMF (0.2% LiBr, 70 °C). For aqueous SEC, two 8 μm, mixed-M bed, 7.5 mm I.D. x 30 cm PL aquagel-OH columns in series (Agilent Technologies) were run in sequence using an isocratic

method with a flow rate of 1.0mL/min in water (0.2M $NaNO_3$ in 0.01M Na_2HPO_4, pH = 7.0). Flow cytometry analysis was performed on live CHO cells using a FACSCalibur (BD Biosciences).

1-(3-methoxy-4-(prop-2-yn-1-yloxy)phenyl)ethan-1-one (2). Reaction protocol adapted from Kaneko, 2011. 25 mL round bottom flask was dried under high vac with a magnetic stir bar. Acetovanillone **1** (0.167 g, 1 mmol, 1 eq) was added to the flask and dried. Anhydrous acetonitrile (0.47 M) was added under nitrogen to dissolve starting material. Potassium carbonate (0.276 g, 2 eq), potassium iodide (0.007 g, 0.04 eq) and 3-bromoprop-1-yne (0.11 mL, 1.45 eq) were subsequently added. The solution was refluxed at 85 °C for 24 hr under nitrogen atmosphere. Reaction progress was monitored by TLC (1:1 Hexane/DCM). After filtration, the organic solvent was evaporated under reduced pressure and the residue was purified by silica gel chromatography using Hexane/DCM (1:1) to deliver the functionalized product **2** (0.193 g, 95%).

1-(5-methoxy-2-nitro-4-(prop-2-yn-1-yloxy)phenyl)ethan-1-one (3). Reaction protocol adapted from Govan, 2013. 25 mL round bottom flask was dried under high vac with a magnetic stir bar. Product **2** (0.193 g, 0.945 mmol, 1 eq) was dried and then dissolved in ice-cold concentrated HNO_3 (1.89 mL, 2 M) for 4 h and slowly warmed up to room temperature overnight. The solution was then poured into ice-cold de-ionized water (200 mL), and the yellow precipitate was filtered off. The filtrate was discarded, and the yellow solid was redissolved in DCM (3.5 mL). Product solution was subsequently washed with saturated aqueous $NaHCO_3$ (2 mL) and saturated NaCl (2 mL) and was dried with anhydrous sodium sulfate. After filtration, the organic solvent was evaporated under reduced pressure and the

residue was purified by silica gel chromatography using DCM/hexane (7:3) to deliver the corresponding nitrobenzyl-ketone **3** (0.157 g, yield 66%).

1-(5-methoxy-2-nitro-4-(prop-2-yn-1-yloxy)phenyl)ethan-1-ol (4). Reaction protocol adapted from Kaneko, 2011. 25 mL round bottom flask was dried under high vac with a magnetic stir bar. Product **3** (0.156 g, 0.628 mmol, 1eq) was dried and then dissolved in a THF (13 mL, 0.3 M) and methanol (26 mL, 0.24 M) mixture in the flask. The solution was cooled to 0°C in an ice bath, and sodium tetrahydroborate (0.166 g, 7eq) was added. The solution was subsequently stirred on the ice bath for 3 hr. Reaction progress was monitored by TLC (1:1 EtOAc/Hexane). After concentrating the solution on a rotary evaporator, H_2O (60 mL) and 2 M HCl (6 mL) were added, and the aqueous solution was extracted with chloroform (3 × 60 mL). The organic layer was dried over magnesium sulfate. After filtration, the organic solvent was evaporated under reduced pressure and the residue was purified by silica gel chromatography using EtOAc/Hexane (1:1) to deliver the reduced product **4** (0.0809 g, 51%).

2,5-dioxopyrrolidin-1-yl (1-(5-methoxy-2-nitro-4-(prop-2-yn-1-yloxy)phenyl)ethyl) carbonate (5). Reaction protocol adapted from Kaneko, 2011. 25 mL round bottom flask was dried under high vac with a magnetic stir bar. Vacuum-dried product **4** (0.0809 g, 0.322 mmol, 1 eq) was dissolved in anhydrous acetonitrile (20 mL) in the flask. Triethylamine (0.14 mL, 3 eq) was added to the solution, followed by *N,N*-Disuccinimidyl carbonate (DSC) (0.247 g, 3 eq). The solution was stirred at room temperature for 24 hr under nitrogen atmosphere. Reaction progress was monitored by TCL (1:2 EtOAc/Hexane). After concentrating the solution on a rotary evaporator, H_2O (30 mL) and 2 M HCl (3.5 mL) were added, and the aqueous solution was extracted with chloroform (3 × 50 mL). The organic layer was washed with saturated

$NaHCO_3$ (3 × 100 mL) and dried over magnesium sulfate. After filtration, the organic solvent was evaporated under reduced pressure and the residue was purified by silica gel chromatography using EtOAc/Hexane (1:2) to deliver the functionalized product **5** (0.036 g, 81%).

Synthesis of 5-Hexynoic NHS Ester (7). 25 mL round bottom flask was dried under high vac with a magnetic stir bar. NHS (16.2 mg, 0.141 mmol, 1.05 eq) and anhydrous DCM (0.67 mL, 0.2 M) were added to the flask under nitrogen. The solution was capped and subsequently cooled to 0°C in an ice bath. 5-hexyanoic acid (0.015 g, 14.8 µL, 0.134 mmol, 1 eq) was added, followed by DIC (21.61 µL, 0.138 mmol, 1.03 eq). The reaction was stirred for 7 hr at room temperature. Reaction progress was monitored by TLC (2:3 EtOAc/Hexane). Product solution was washed with 0.1M HCl, saturated aqueous $NaHCO_3$ and saturated NaCl. Aqueous phase was backextracted with DCM (3 x 0.3 mL), and combined organic phase was subsequently dried with anhydrous sodium sulfate. After filtration, the organic solvent was evaporated under reduced pressure and the residue was purified by silica gel chromatography using EtOAc/Hexane (2:3) to deliver the functionalized product **7** (0.085 g, 90%).

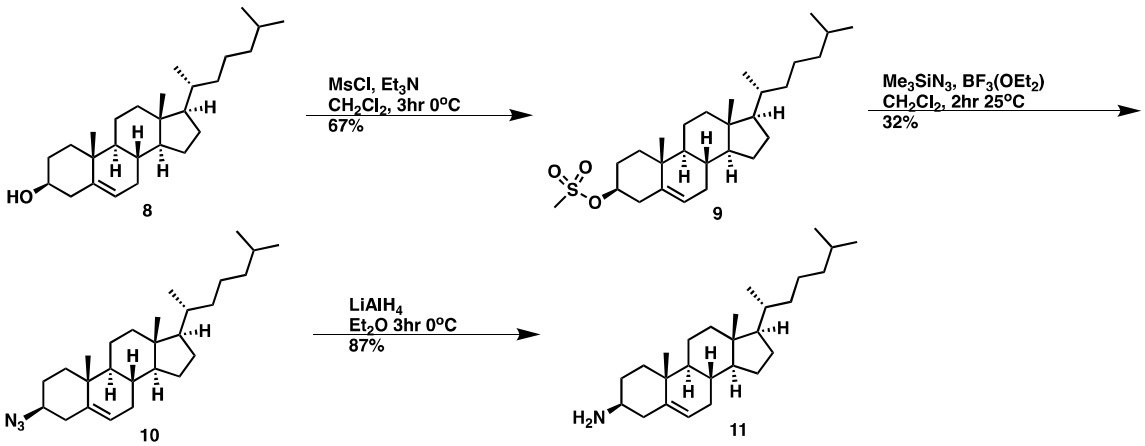

Figure 5 Reprint.

Synthesis of 3ß-cholest-5-en-3-amine (11). 3ß-cholest-5-en-3-amine (**Fig 5 Reprint**) was prepared according to published procedures as detailed by Isabettini, 2017.

Synthesis of cholesterol-nitrobenzyl endgroup (12). 4 mL glass vial was dried under high vac with a magnetic stir bar. Equimolar nitrobenzyl-linker **(5)** (0.0357 g, 0.091 mmol, 1eq) and cholesterol-amine **(11)** (0.0352 g, 0.091 mmol, 1eq) were dried and combined in the vial. THF (0.5 mL, 0.2 M) was added and the reaction was stirred at room temperature for 18hr. Reaction progress was monitored by TLC (1:4 Hexane/DCM, CAM stain). The solution was evaporated under reduced pressure and the residue was purified by silica gel chromatography using Hexane/DCM (1:4) to deliver the conjuagted product **12** (0.0603 g, 60%).

Synthesis of cholesterol-hexynoic acid endgroup (13). 4 mL glass vial was dried under high vac with a magnetic stir bar. Equimolar hexynoic acid-linker **(7)** (0.0263 g, 0.126 mmol, 1eq) and cholesterol-amine **(11)** (0.0485 g, 0.126 mmol, 1eq) were dried and combined in the vial. THF (0.63 mL, 0.2 M) was added, and the reaction was stirred at room temperature for 18hr. Reaction progress was monitored by TLC (1:4 EtOAc/Hexane, CAM stain and $KMnO_4$ stain). The solution was evaporated under reduced pressure and the residue was purified by silica gel chromatography using EtOAc/Hexane (1:4) to deliver the conjuagted product **12** (0.0449 g, 74%).

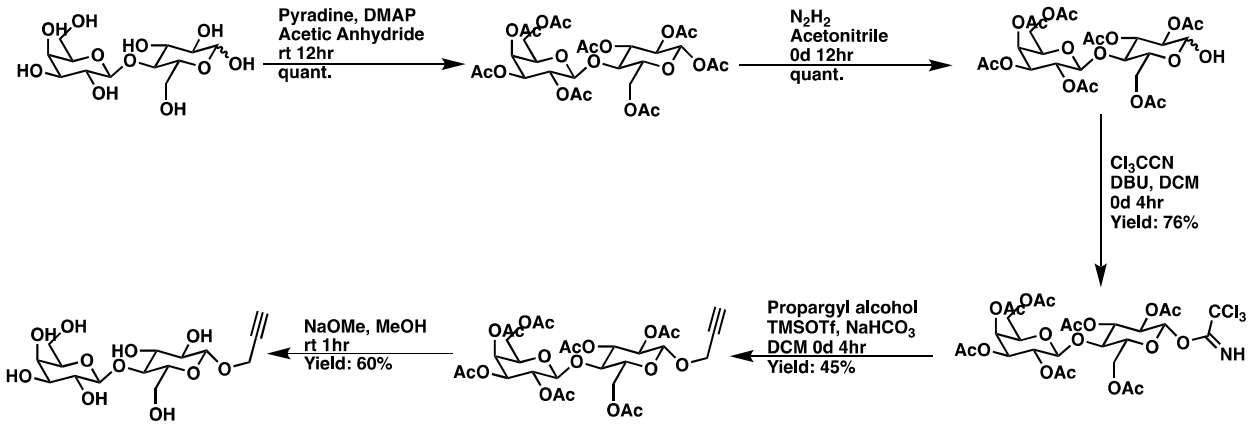

Figure 19: Synthesis scheme of ß-propargyl lactoside **14**

Synthesis of ß-propargyl lactoside (14). Propargyl lactoside (**Fig 19**) was prepared according to published procedures on Schmidt glycosylation as detailed by Honigfort, 2019.

Synthesis of azide-terminated poly(epichlorohydrin), pECH (P1). Epichlorohydrin was polymerized according to the procedure developed by Carlotti and detailed by Honigfort, 2019. Briefly, a flame-dried 10 mL Schlenk flask equipped with a magnetic stirrer and fitted with PTFE stopcock was charged with tetrabutylammonium azide ($TBAN_3$, 30 mg, 0.055 mmol, 0.003 equiv.) under argon. A solution of freshly distilled epichlorohydrin (1.29 mL, 16.5 mmol) in anhydrous toluene (4 mL) was added. A solution of triisobutylaluminum in toluene (1.07 M, 104 µL, 0.111 mmol, 0.007 equiv.) was added via a syringe under argon at −30 °C. The reaction was stirred for 4 hr and then stopped by the addition of ethanol. The resulting pECH polymer **(P1)** was precipitated into hexanes and dried under vacuum to yield a clear viscous oil (1500 mg, 99 % yield). The polymer was analyzed by SEC (0.2% LiBr in DMF): M_w = 29,000, M_n = 27,700, Đ = 1.23).

Synthesis of endgroup-terminated poly(epichlorohydrin) (Endgroup-P1). Reaction protocol adapted from Honigfort, 2019. In a vacuum-dried 4 mL glass vial, pECH polymer **P1** (7.5 mg, 0.25 µmol, 1eq) was dissolved in degassed anhydrous DMSO (500 µL) with a magnetic stir bar. Cholesterol-nitrobenzyl endgroup **12** (1.7 mg, 2.5 µmol, 10 eq), cholesterol-hexynoic acid endgroup **13** (1.2 mg, 2.5 µmol, 10 eq), or no endgorup was added, followed by CuI (~0.05mg, 0.3 µmol, 1.0 equiv.) and one drop diisopropylethyl amine (DIPEA, ~ 5 µL). The reaction was stirred at 40°C for 12 hr, at which time it was quenched by the addition of DCM and treated with Cuprisorb beads (SeaChem labs) for 18 hrs to sequester copper. The resulting copper-free solutions were filtered through celite to remove the resin and evaporated on the rotary evaporator and vacuum. The dried residues were triturated 3-4X with 30% choloroform/EtOH and monitored with TLC to remove excess unreacted **12** or **13**. The resultant polymers were dried under vasuum to yield **Chol-Photo P1** (7.2 mg, 96%), **Chol P1** (6.7mg, 89%), and **No Engroup** P1 (7.0mg, 93%).

Synthesis of endgroup-terminated poly(glycidyl azide), pGA (Endgroup P2). Reaction protocol adapted from Honigfort, 2019. In vacuum-dried 4 mL glass vials, endgroup functionalized polymers **Endgroup-P1** (6.7 - 7.2 mg, 0.22-0.24 µmol, 1eq) were dissolved in anhydrous DMF (200 µL) with a magnetic stir bar. To the solution was added NaN_3 (~2.0 mg, 2.0 equiv.), and the reaction was stirred at 60 °C for 3 days under argon to allow complete conversion. Polymer solution was filtered to remove solids and evaporated to remove DMF. Dried residue was dissolved in DCM, and any solid in solution was filtered off; avoided vigorous shaking before filtration. Solution was evaporated to yield the product endgroup functionalized p(GA) polymers **Endgroup P2** (6.6 - 7.71mg, 93%). The polymers were analyzed by SEC (0.2% LiBr in DMF): M_w = 29,000, M_n = 29,200-30,600, Đ = 1.19-1.21 (**Fig 8**).

Synthesis of Cy5-labeled glycopolymers 5. Reaction protocol adapted from Honigfort, 2019. In vacuum-dried 4 mL glass vials, endgroup functionalized p(GA) polymers **Endgroup P2** (7.50 mg, 0.075 mmol) were dissolved in degassed dry DMSO (250 µL) with a magnetic stir bar. To the solution was added Cy5-alkyne (7.5 mg, 0.75 µmol) in DMSO (75 µL), followed by CuI (1.67 mg, 7.50 µmol) and DIPEA (13.3 uL, 0.075 mmol). The reaction was stirred in dark under Ar at 40 °C for 2 hrs. After this time, propargyl lactosides **14** were added to the reaction mixture (0.113 mmol, 1.5 eq per azide side-chain) in degassed anhydrous DMSO (50 µL). The reactions were stirred in dark at 40°C overnight. After this time, the reactions were diluted with DI water and treated with Cuprisorb beads (SeaChem labs) for 18 hrs to sequester copper. The resulting copper-free solutions were filtered through celite to remove the resin and lyophilized. The dry residues were triturated 3x with methanol with monitoring by TLC to remove excess unreacted glycosides. The resulting Cy5-labeled glycopolymers **5** were dissolved in D_2O and lyophilized to give a blue solid in a quantitative yield for each polymer (*note*: the blue color of the glycopolymers arises from the presence of the Cy5 label and not residual copper contamination. Glycopolymers lacking the Cy5 label were isolated as white solids). The polymers **5** were characterized using ^{1}H NMR ($CDCl_3$, 300 MHz) and UV-Vis (λ_{max} = 633 nm) spectroscopy. Absorbance readings at known concentrations of glycopolymers **Endgroup GP** indicating the presence of ~ 1 Cy5 molecules per polymer chain (0.2% sidechain occupancy).

Remodeling the glycocalyx of suspended CHO-Lec8 cells with varying concentrations of glycopolymers and quantification by flow cytometry. CHO Lec8 cells (100,000 cells/condition) were incubated with Cy5-labeled lactosyl-polymers (**Chol-Photo GP, Chol GP, No Endgroup GP**) at varying concentrations (c_{pol} = 0.625 µM, 1.25 µM, 2.5 µM, 5 µM,10 µM, 20 µM) in 1.7

mL Eppendorf tubes. Cells-only was included as a control and received equal treatment. In effect, 100,000 cells were suspended in 50 µL basal growth media (Mem-1-alpha) for every condition, and polymer was diluted into this solution from a 500 µM stock. The cells were incubated at 4°C for an hour on the rotisserie shaker. After incubation, the cells are centrifuged at 400xg for 5 minutes to pellet. Supernatant containing excess polymer was removed, and the cells are washed 3X with 50 µL DPBS to remove residual polymer. Then the cells were resuspended in 500 µL DPBS and probed for the presence of Cy5 fluorescence using flow cytometry. The data were analyzed on FlowJo online software. Cells were gated to exclude debris, and the median fluorescence intensities (MFI) of cells are reported. Means and standard deviations for each condition were calculated from three independent biological replicates.

Photocleavage of glycopolymer following incorporation and quantification by flow cytometry. CHO Lec8 cells (100,000 cells/condition) were incubated with Cy5-labeled lactosyl-polymers (**Chol-Photo GP, Chol GP**) at 5 µM in a 50 µL solution. Cells-only was included as a control and received equal treatment. The cells were incubated at 4°C for an hour on the rotisserie shaker. After incubation, supernatant containing excess polymer was removed, and the cells are washed 1X with 50 µL DPBS to remove residual polymer. Each sample was transferred to a 5mL polystyrene round bottom flow cytometry tube for UV irradiation. The tubes are rested on ice while a 15-Watt 365nm UV flashlight shines light from above (**Fig 20**). After UV treatment, each sample was diluted to 500 µL with DPBS and probed for the presence of Cy5 fluorescence using flow cytometry. The data were analyzed on FlowJo online software. Cells were gated to exclude debris, and the median fluorescence intensities (MFI) of cells are reported. Means and standard deviations for each condition were calculated from three

independent biological replicates. The linear regions of the photocleavage curves were determined and fitted using a linear regression in PRISM software. The slopes designating the initial rates of photocleavage and the R^2 values for the linear fits were extracted for each condition.

Figure 20: Set-up of UV treatment

ECA lectin staining of glycocalyx-remodeled CHO Lec8 cells and quantification flow cytometry. CHO Lec8 cells (100,000 cells/condition) were incubated with Cy5-labeled lactosyl-polymers (**Chol-Photo GP, Chol GP**) at 5 µM in a 50 µL solution. Cells-only was included as a control and received equal treatment. The cells were incubated at 4°C for an hour on the rotisserie shaker. After incubation, each sample was transferred to a 5mL polystyrene round bottom FACS tube for UV irradiation. After UV treatment, the samples were transferred to 1.7 mL Eppendorf tubes, supernatant containing excess and photocleaved polymer was removed, and the cells are washed 1X with 50 µL DPBS to remove residual polymer. The samples were resuspended in 50 µL DPBS, and fluorescein-labeled ECA was added at sub-agglutination concentrations (c_{ECA} = 12.5 µg/mL). The samples were

subsequently incubated at 4°C for 20 min. After incubation, supernatant containing excess ECA was removed, and each sample was resuspended in 500 µL with DPBS to be probed using flow cytometry for the presence of Cy5 fluorescence. The data were analyzed on FlowJo online software. Cells were gated to exclude debris, and the median fluorescence intensities (MFI) of cells are reported. Means and standard deviations for each condition were calculated from three independent biological replicates, and *p*-values corresponding to each condition vs. untreated control were calculated using 2-way ANNOVA tests with PRISM software. The linear regions of the lectin binding curves were determined and fitted using a linear regression in PRISM software.

APPENDIX

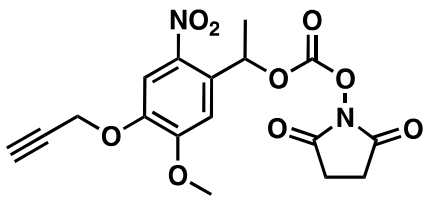

5

Figure A1: Structure of bifunctional nitrobenzyl linker **5**

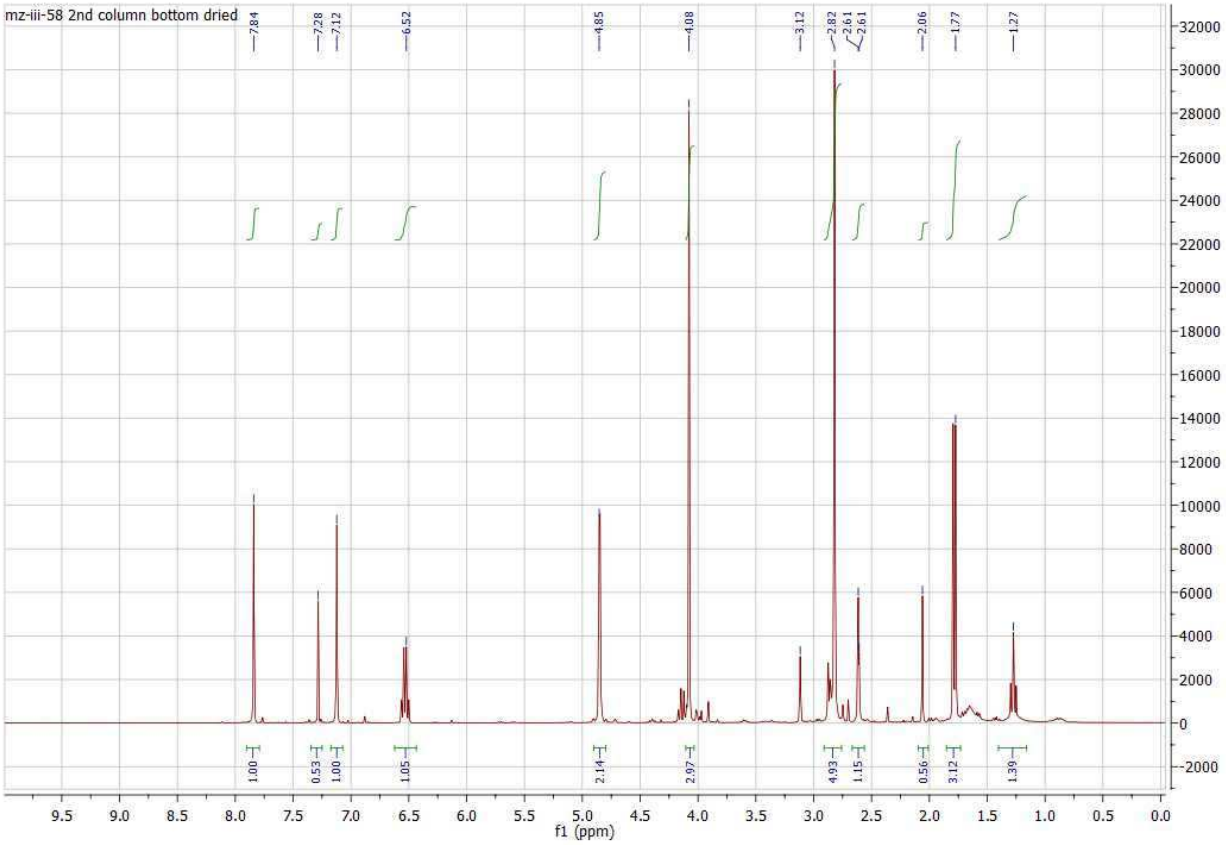

Figure A2: 1H-NMR of bifunctional nitrobenzyl linker **5**

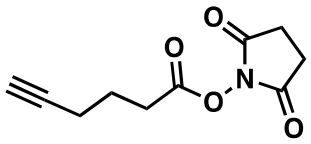

7

Figure A3: Structure of bifunctional hexynoic acid linker **7**

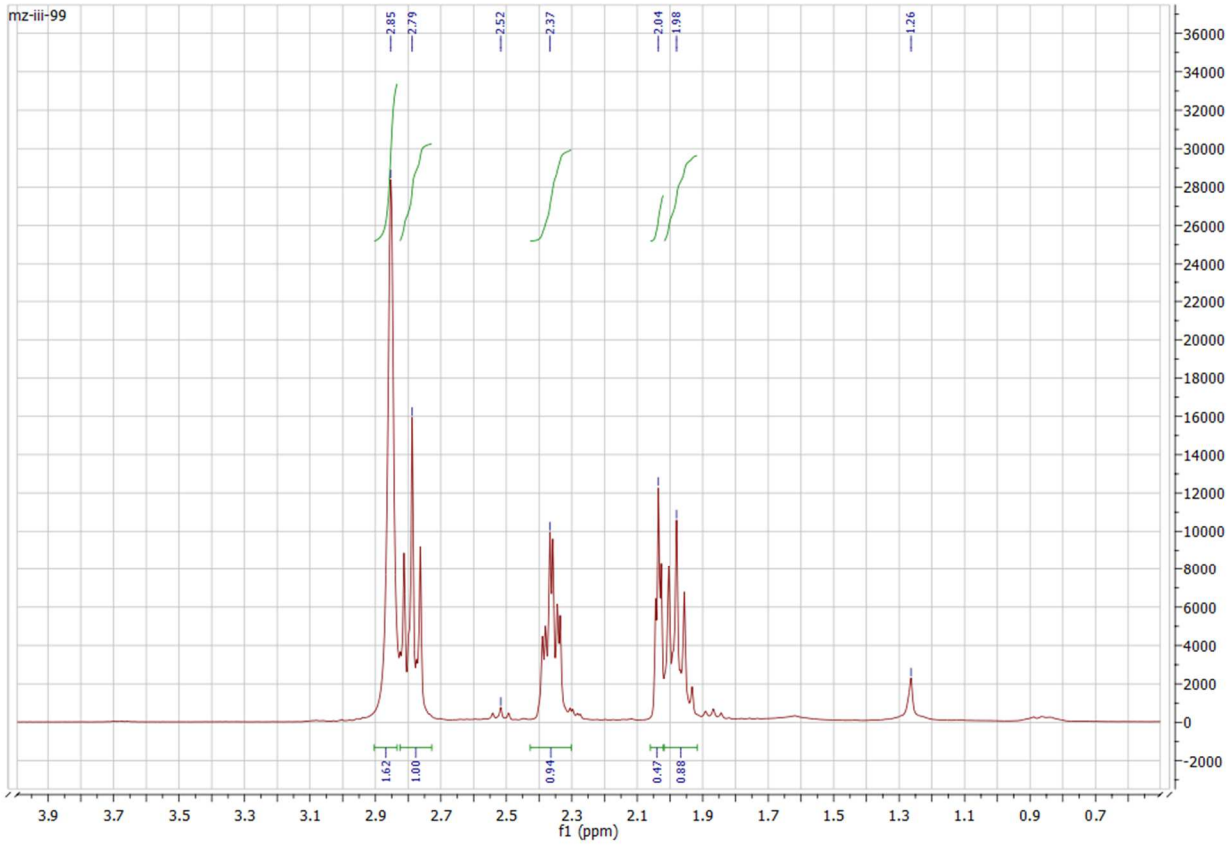

Figure A4: 1H-NMR of bifunctional hexynoic acid linker **7**

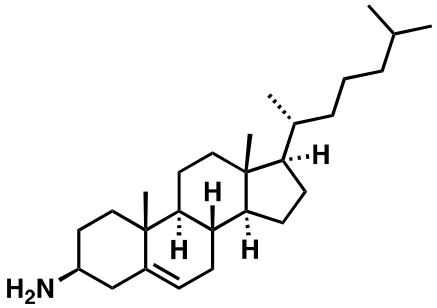

11

Figure A5: Structure of cholesterol-amine **11**

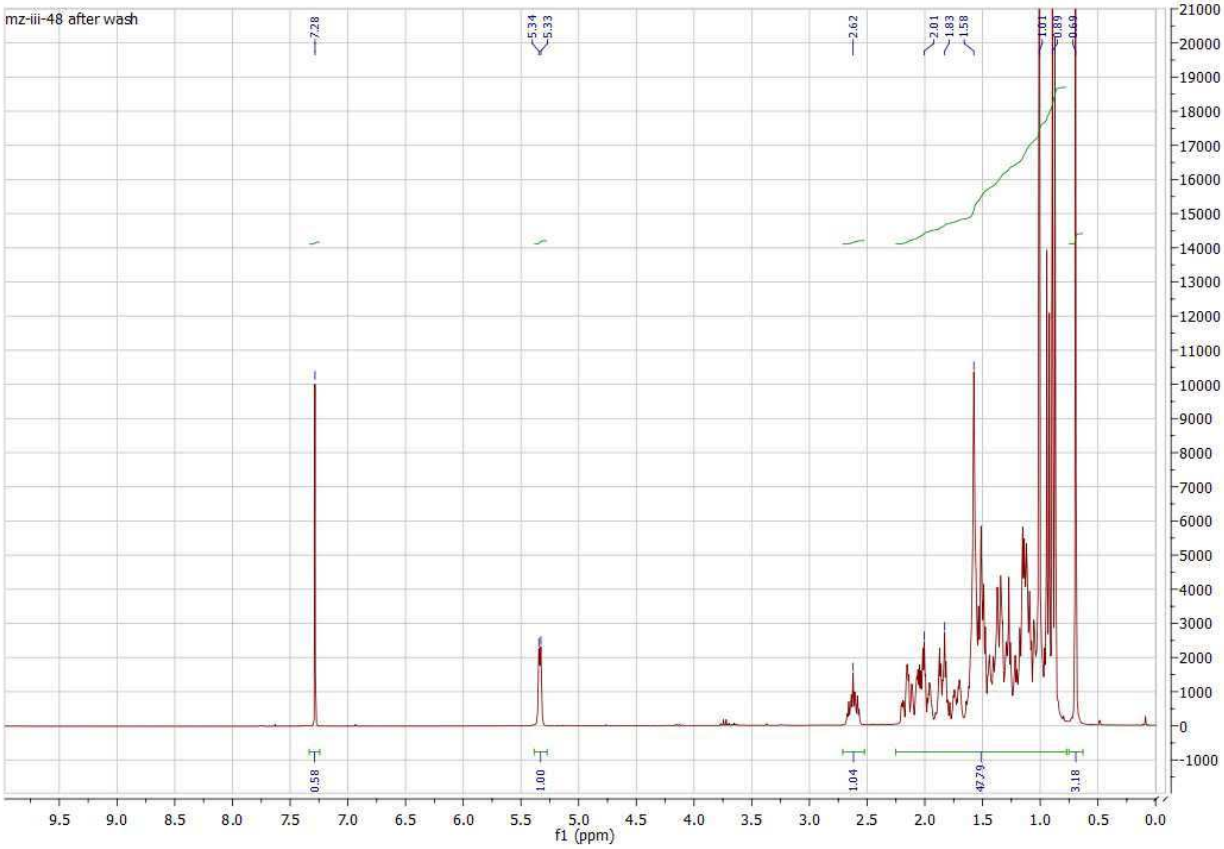

Figure A6: 1H-NMR of cholesterol-amine **11**

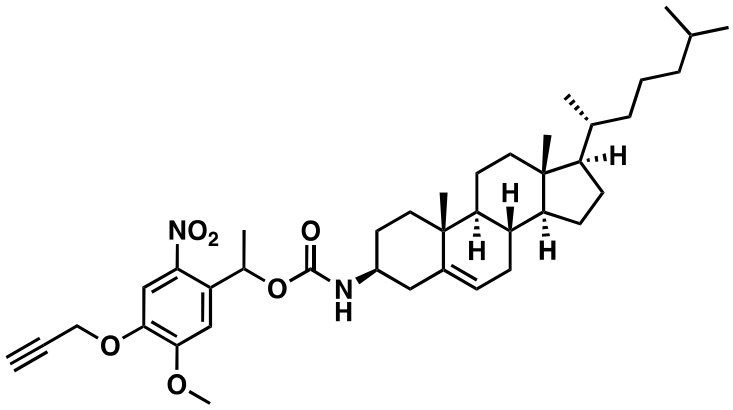

12

Figure A7: Structure of cholesterol-hexynoic acid linker **13**

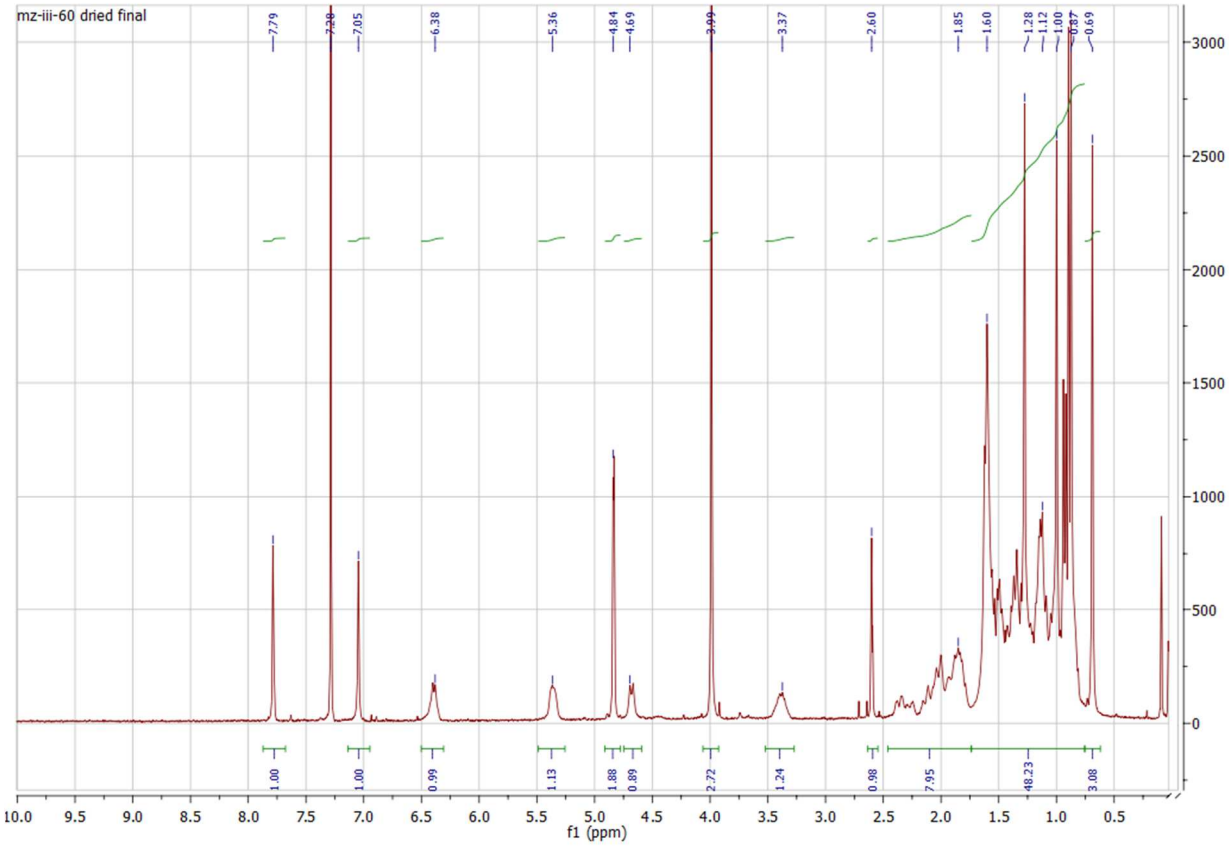

Figure A8: 1H-NMR of cholesterol-nitrobenzyl linker **12**

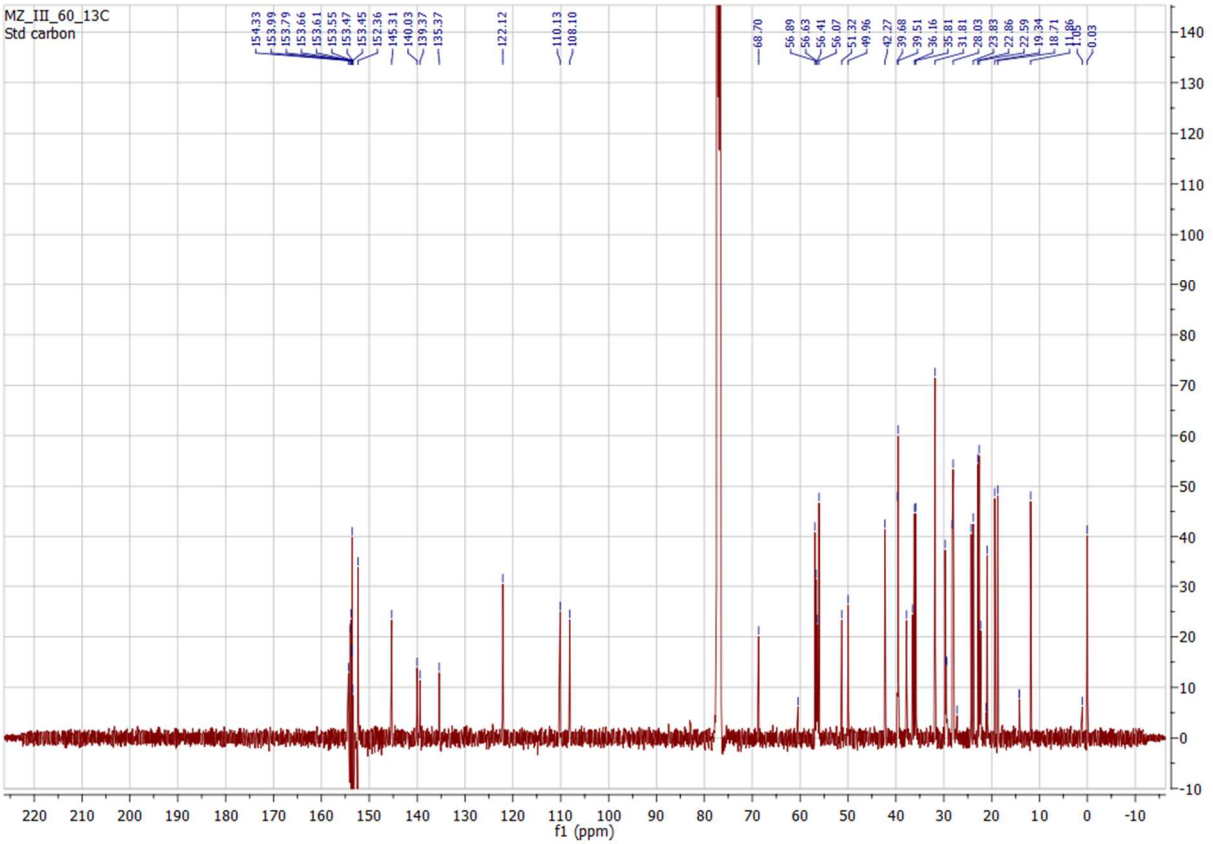

Figure A9: C13-NMR of cholesterol-nitrobenzyl linker **12**

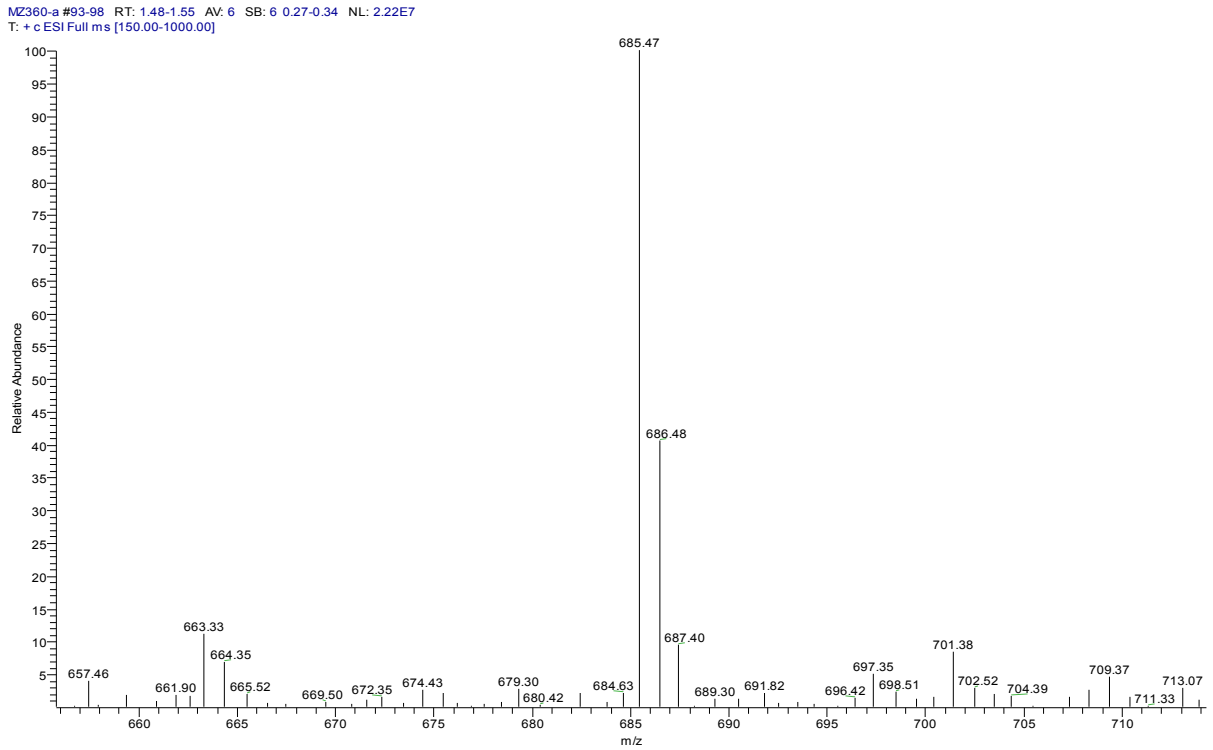

Figure A10: HRMS of cholesterol-nitrobenzyl linker **12**

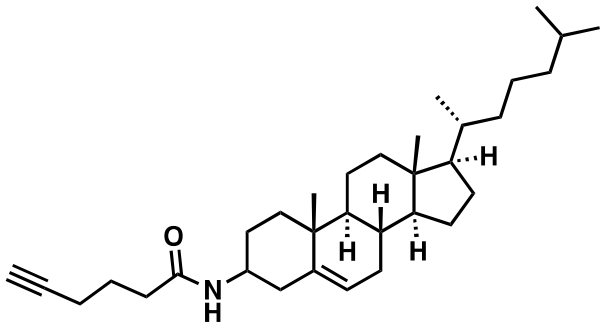

13

Figure A11: Structure of cholesterol-hexynoic acid linker **13**

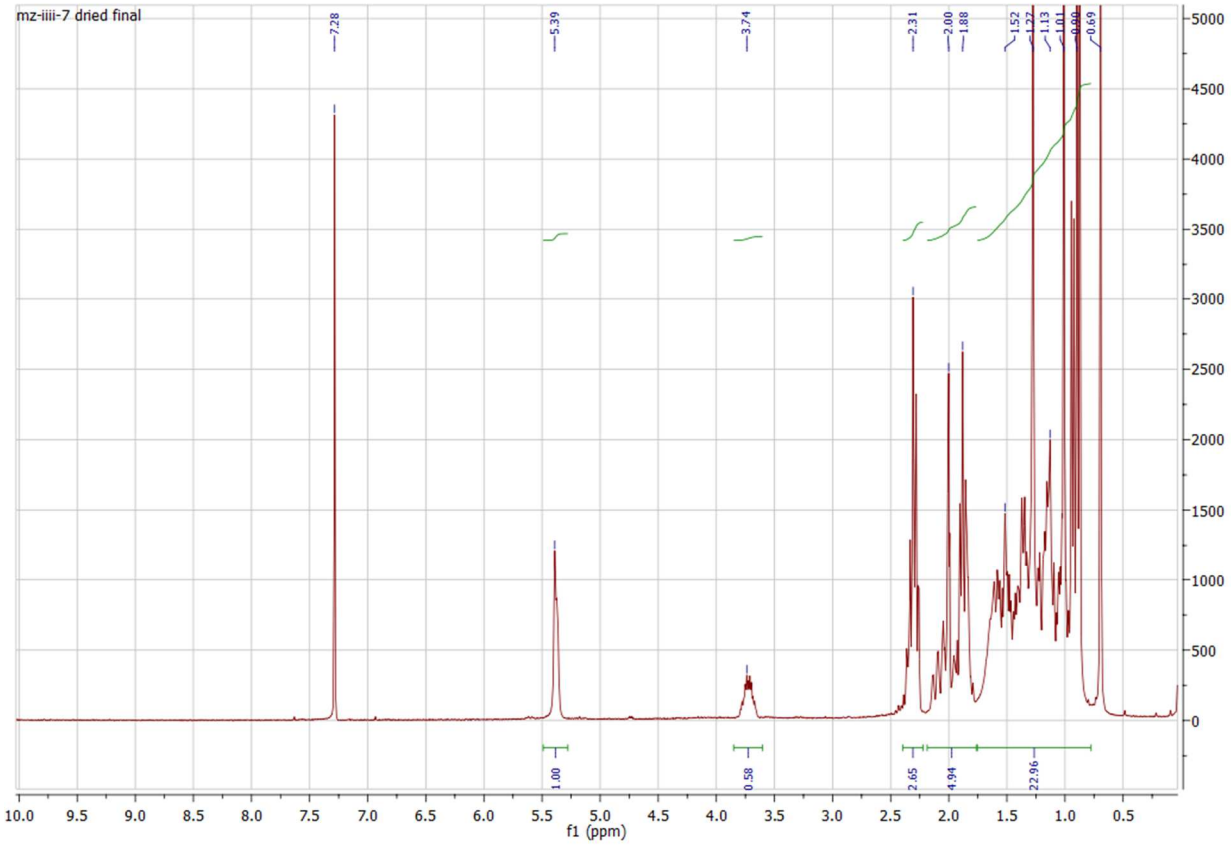

Figure A12: 1H-NMR of cholesterol-hexynoic acid linker **13**

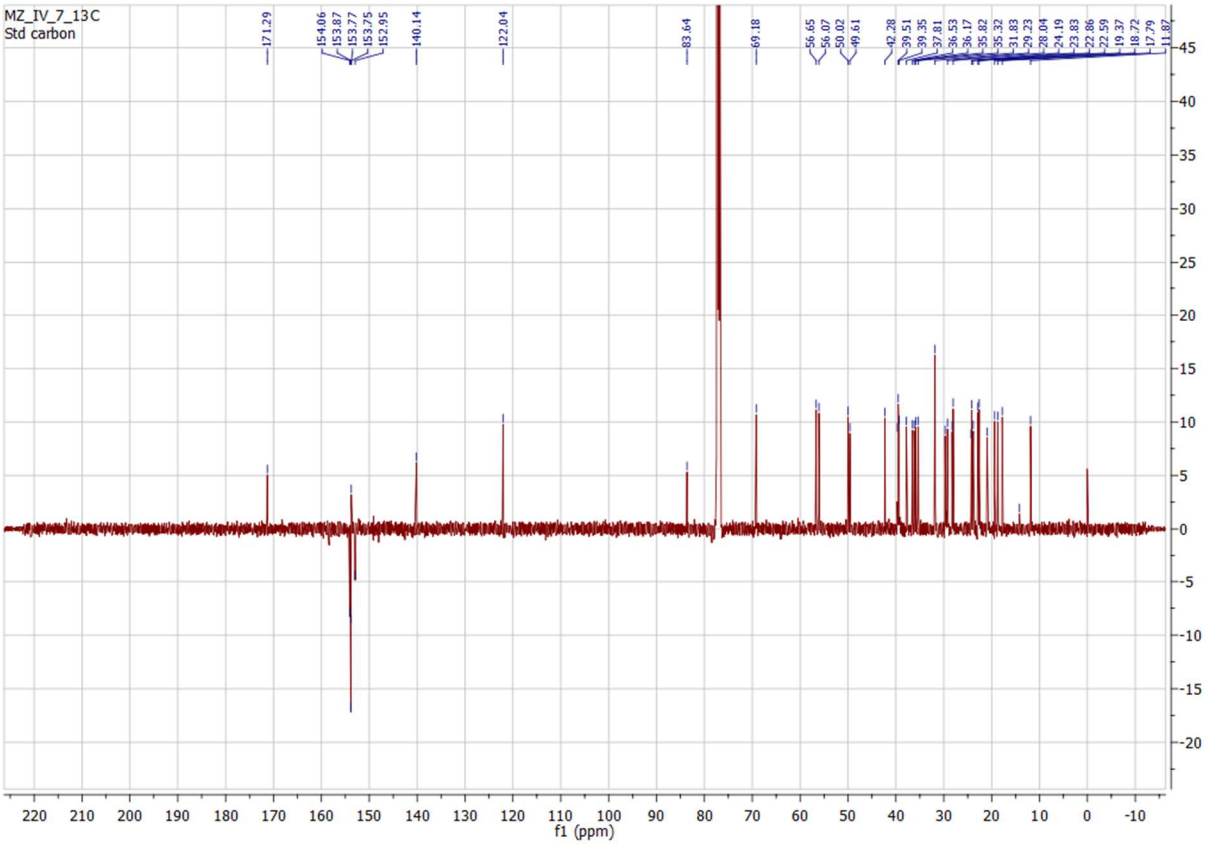

Figure A13: C13-NMR of cholesterol-hexynoic acid linker **13**

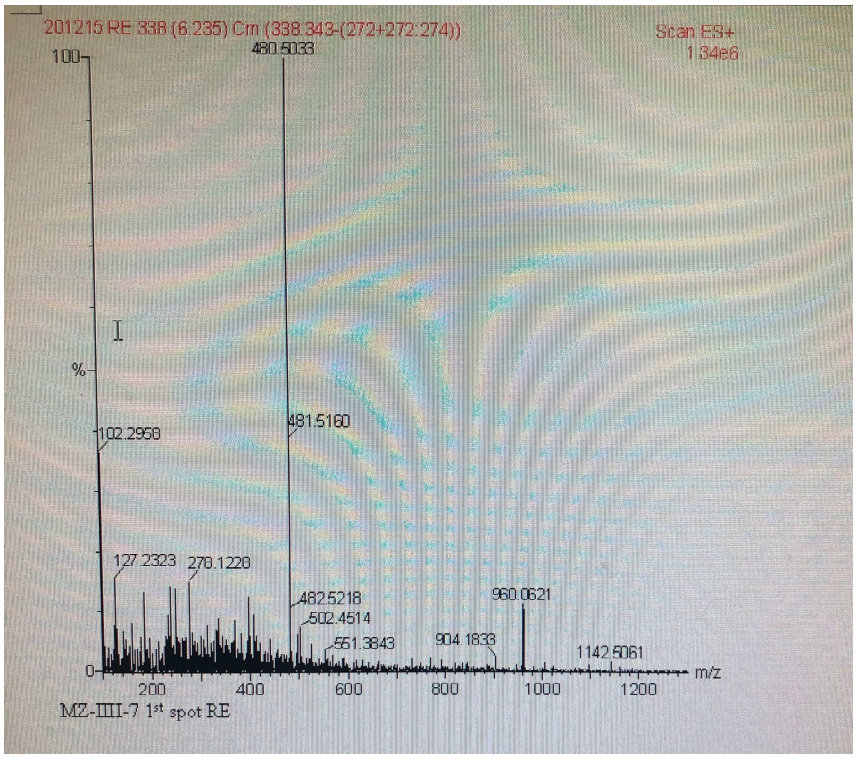

Figure A14: HRMS of cholesterol-hexynoic acid linker **13**

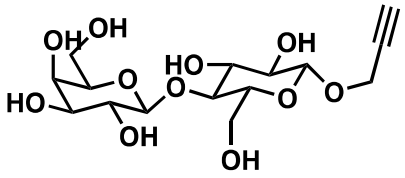

Figure A15: Structure of β-Propargyl Lactosides **14**

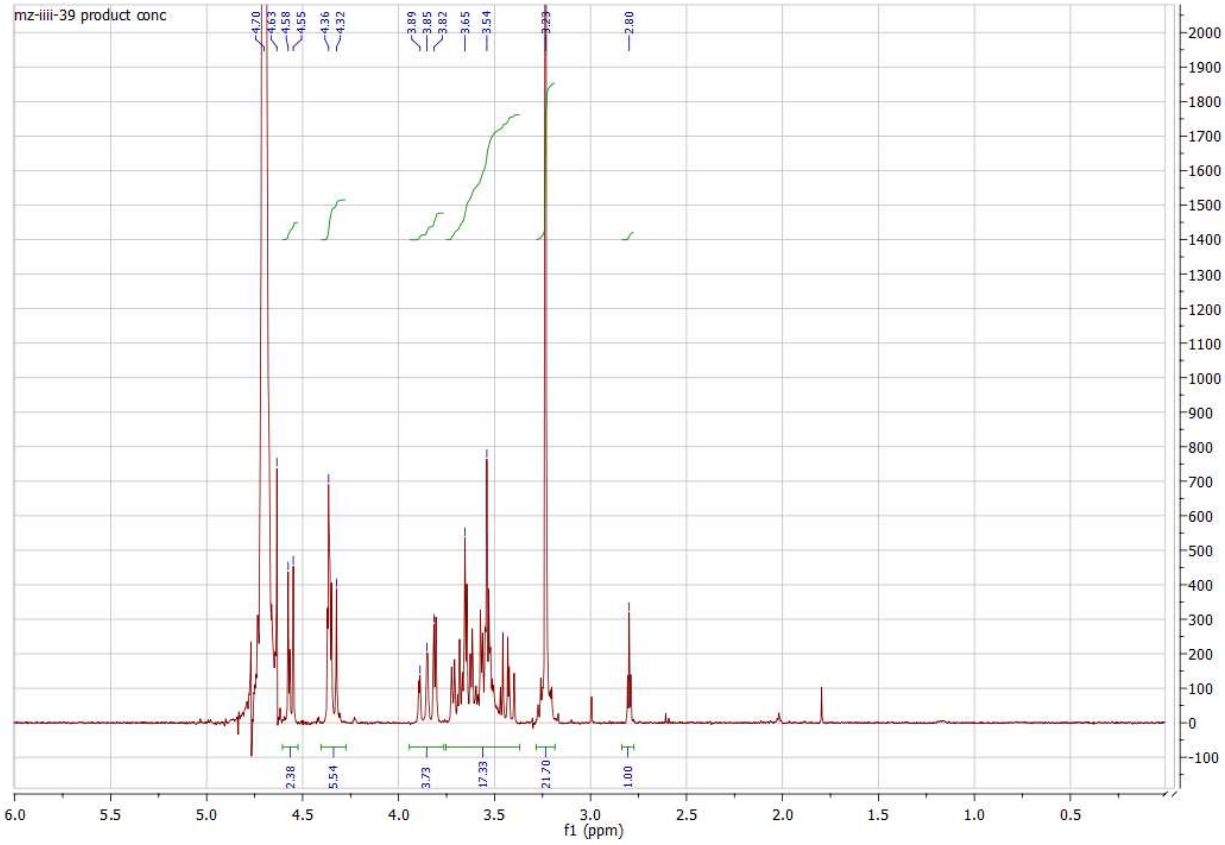

Figure A16: 1H-NMR of β-Propargyl Lactosides **14**

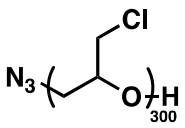

P1

Figure A17: Structure of azide-terminated poly(epichlorohydrin) **P1**

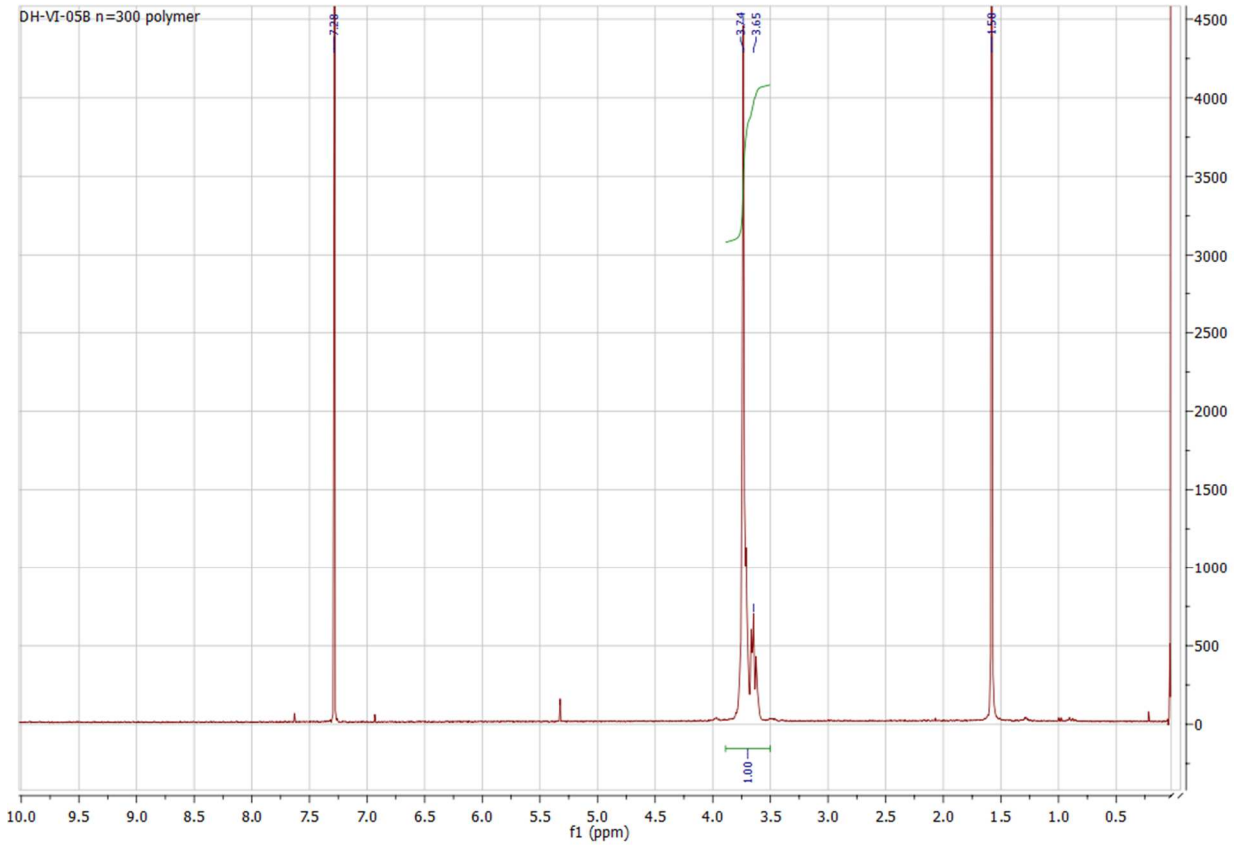

Figure A18: 1H-NMR of azide-terminated poly(epichlorohydrin) **P1**

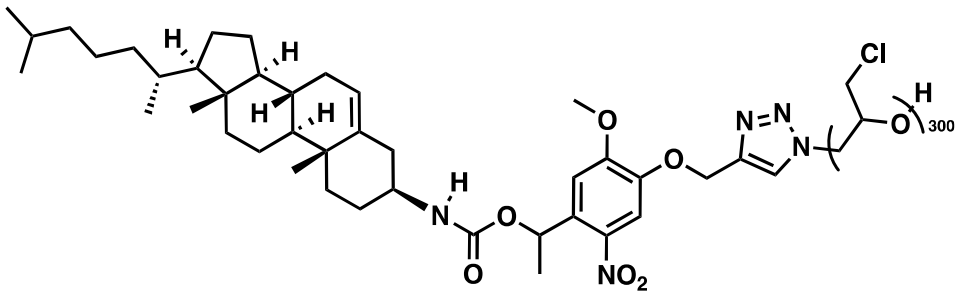

Chol-Photo P1

Figure A19: Structure of cholesterol-nitrobenzyl linker functionalized poly(epichlorohydrin) **P1**

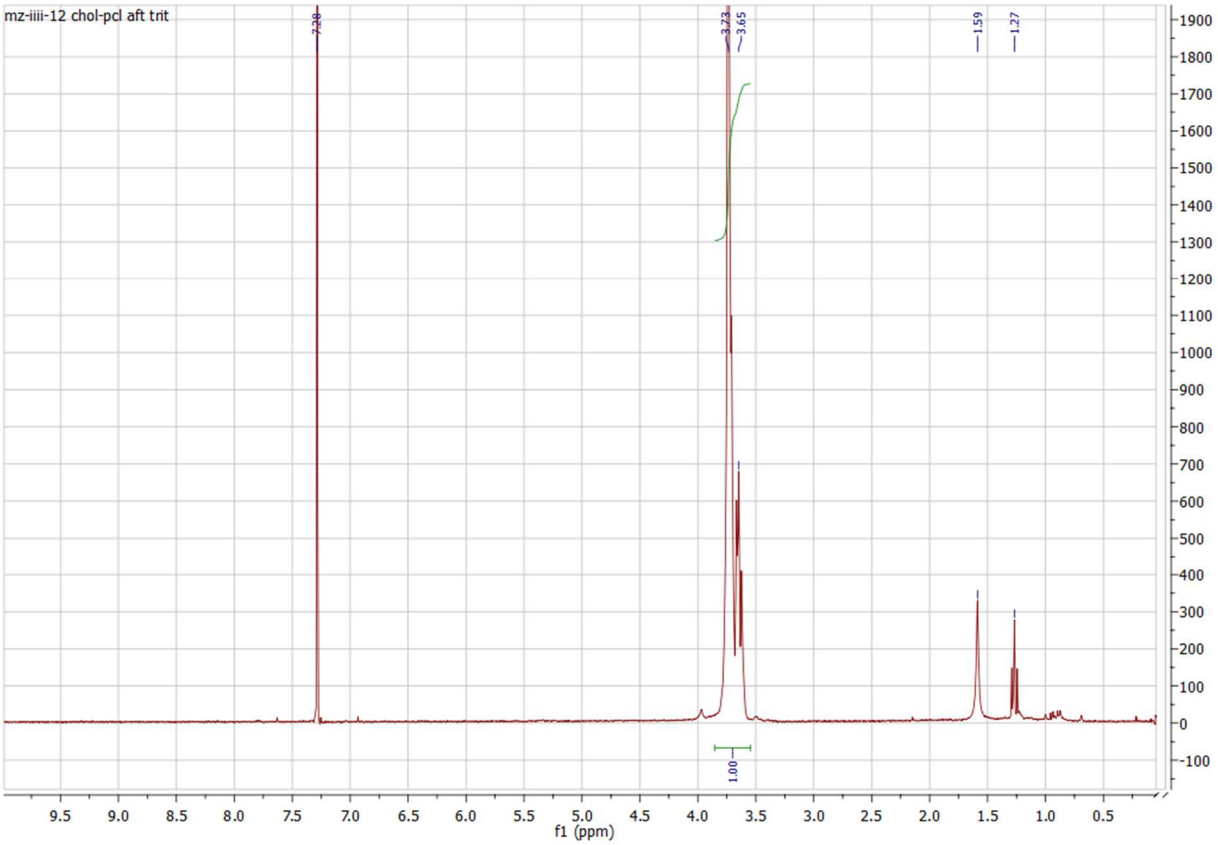

Figure A20: 1H-NMR of cholesterol-nitrobenzyl linker functionalized poly(epichlorohydrin) **Chol-Photo P1**

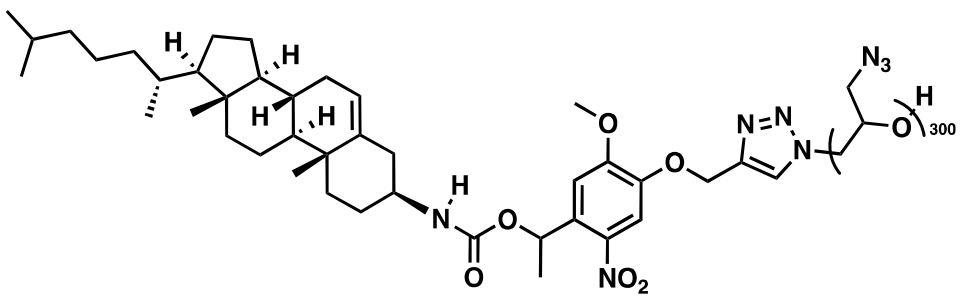

Chol-Photo P2

Figure A21: Structure of cholesterol-nitrobenzyl linker functionalized poly(glycidyl azide) **Chol-Photo P2**

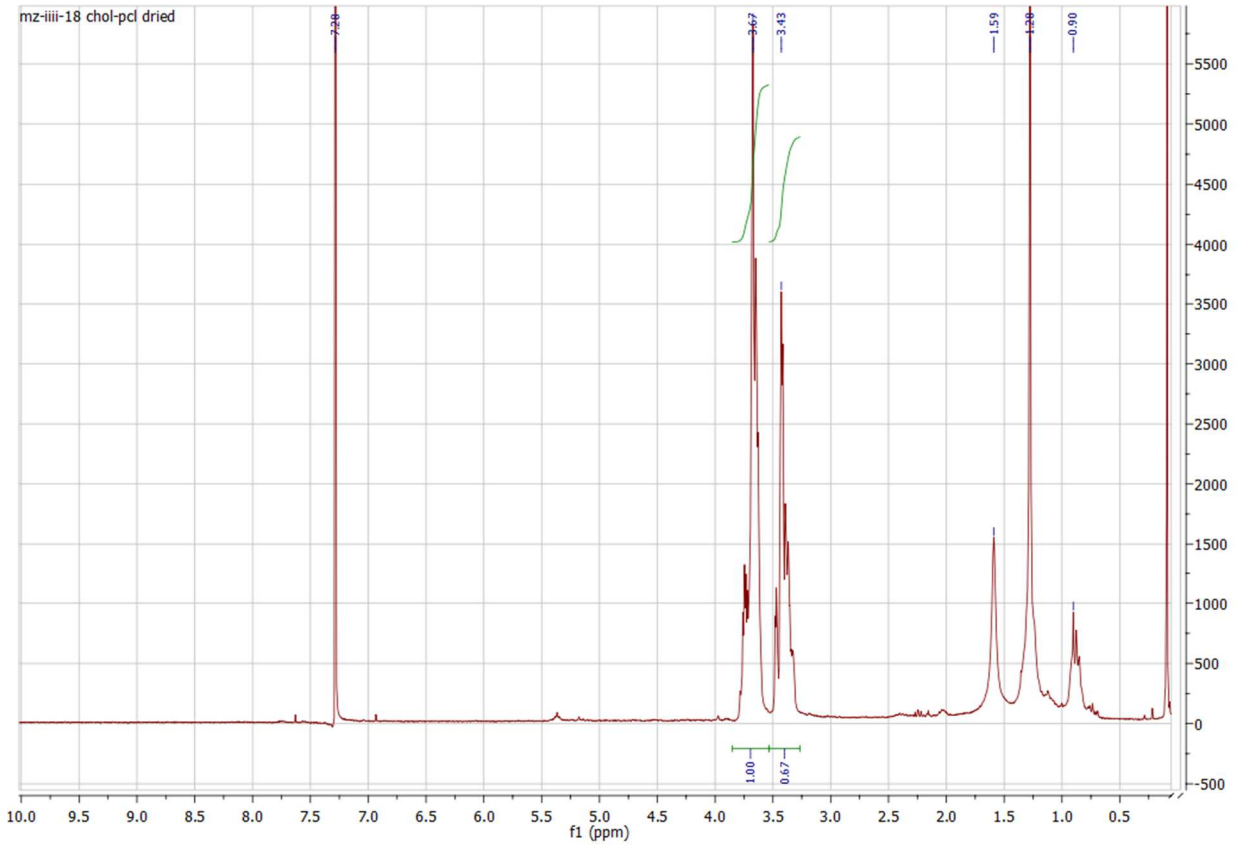

Figure A22: 1H-NMR of cholesterol-nitrobenzyl linker functionalized poly(glycidyl azide) **Chol-Photo P2**

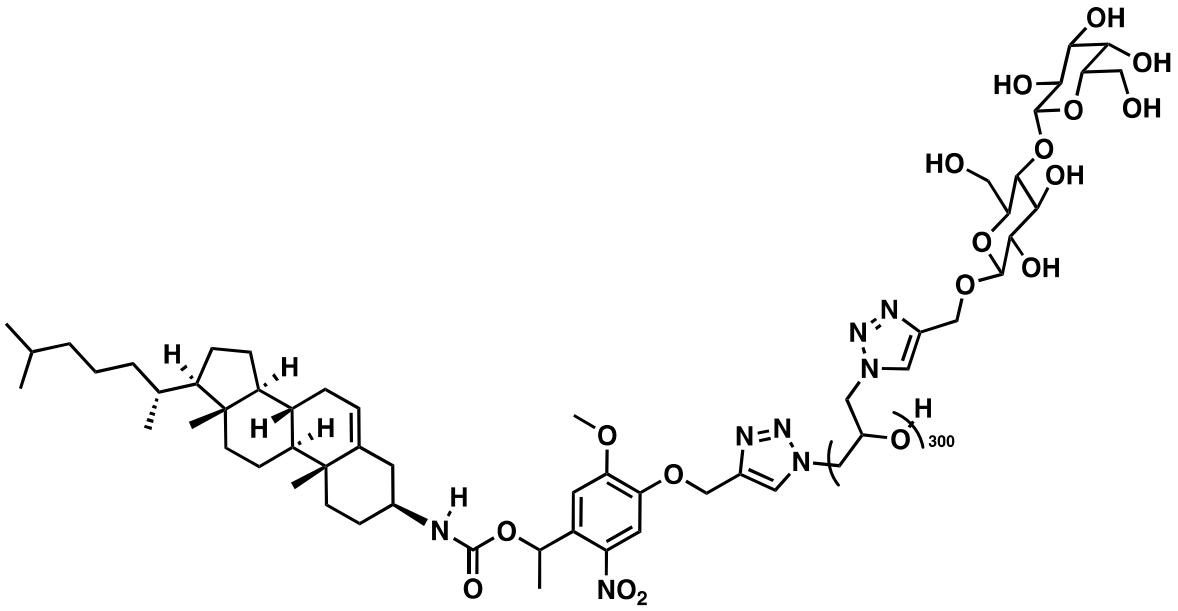

Chol-Photo GP

Figure A23: Structure of cholesterol-nitrobenzyl linker functionalized lactosyl glycopolymer **Chol-Photo GP**

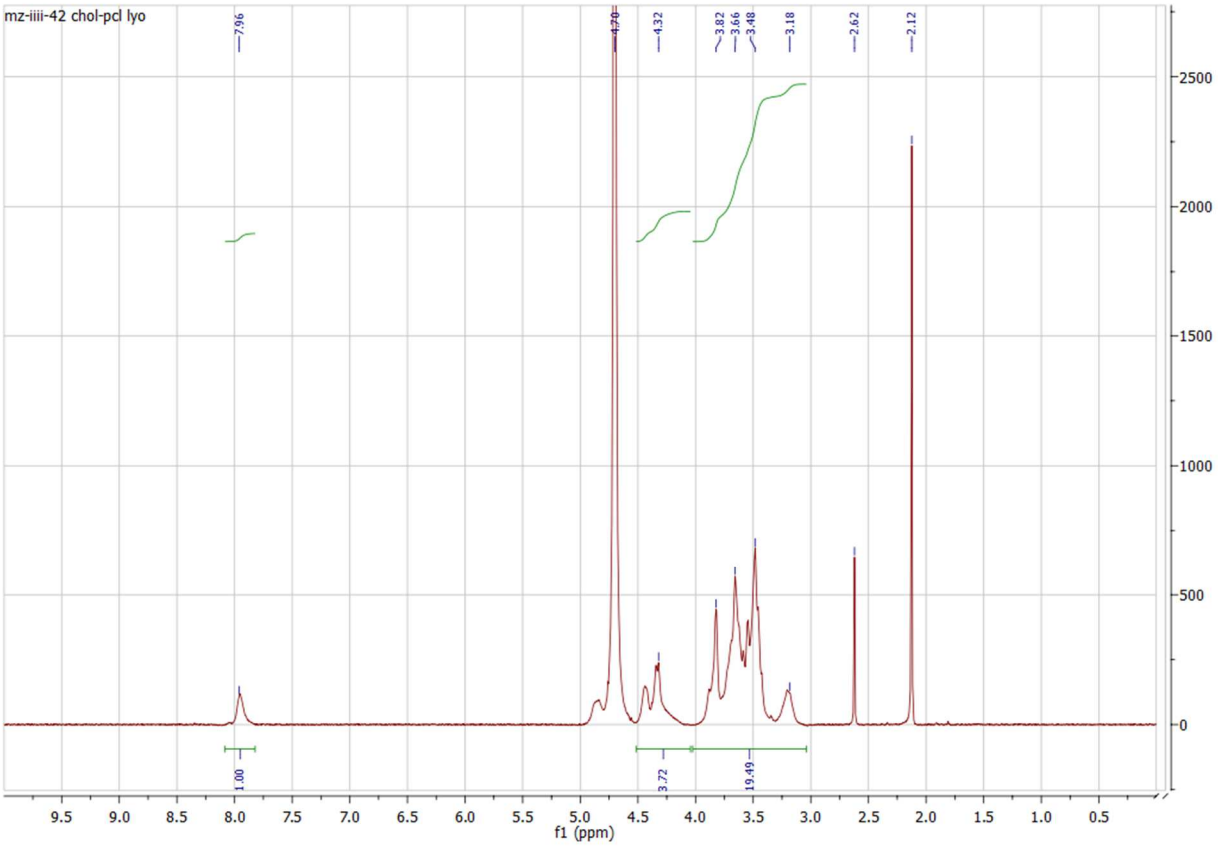

Figure A24: 1H-NMR of cholesterol-nitrobenzyl linker functionalized lactosyl glycopolymer **Chol-Photo GP**

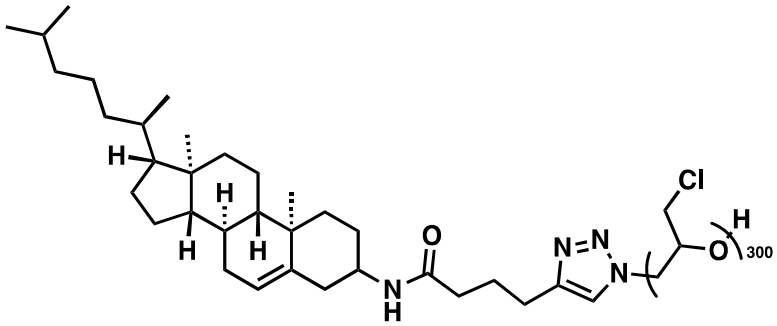

Chol P1

Figure A25: Structure of cholesterol-hexynoic acid linker functionalized poly(epichlorohydrin) **Chol P1**

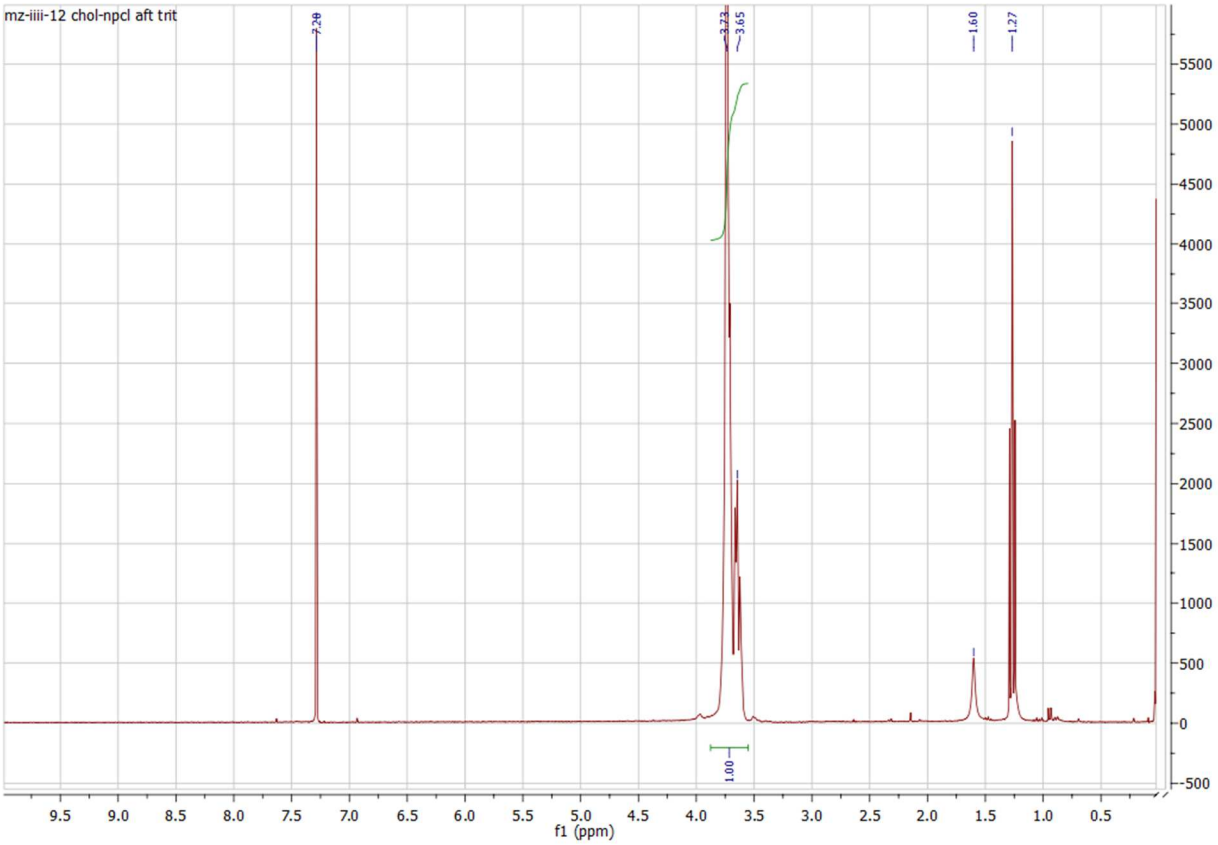

Figure A26: 1H-NMR of cholesterol-hexynoic acid linker functionalized poly(epichlorohydrin) **Chol P1**

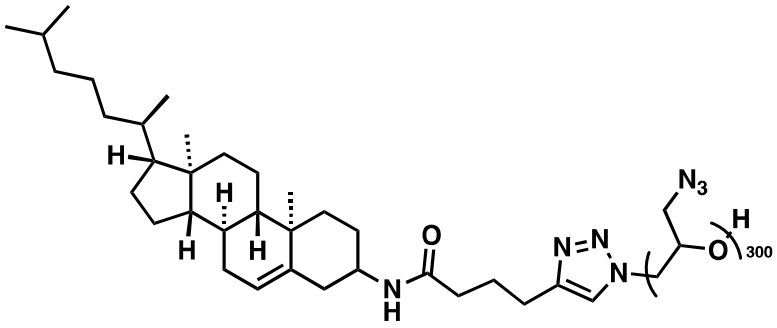

Chol P2

Figure A27: Structure of cholesterol-hexynoic acid linker functionalized poly(glycidyl azide) **Chol P2**

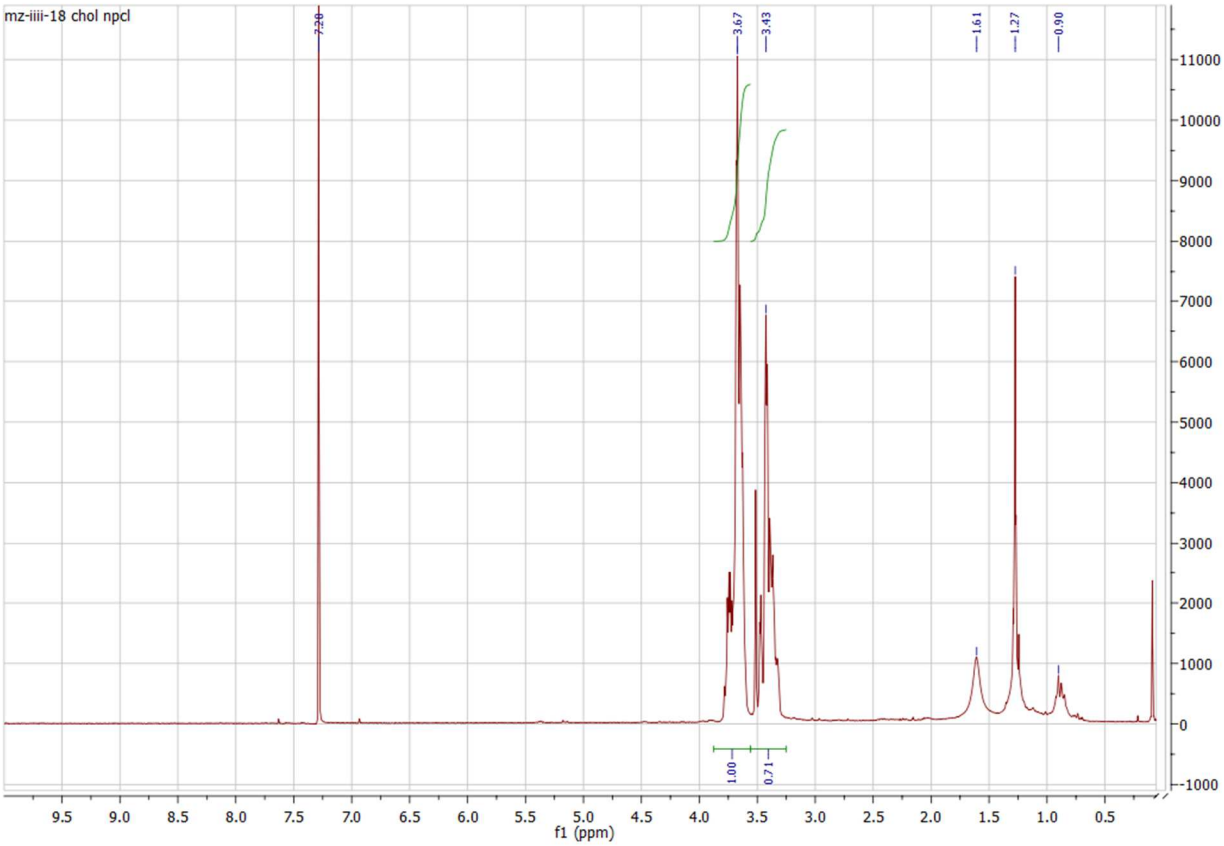

Figure A28: 1H-NMR of cholesterol-hexynoic acid linker functionalized poly(glycidyl azide) **Chol P2**

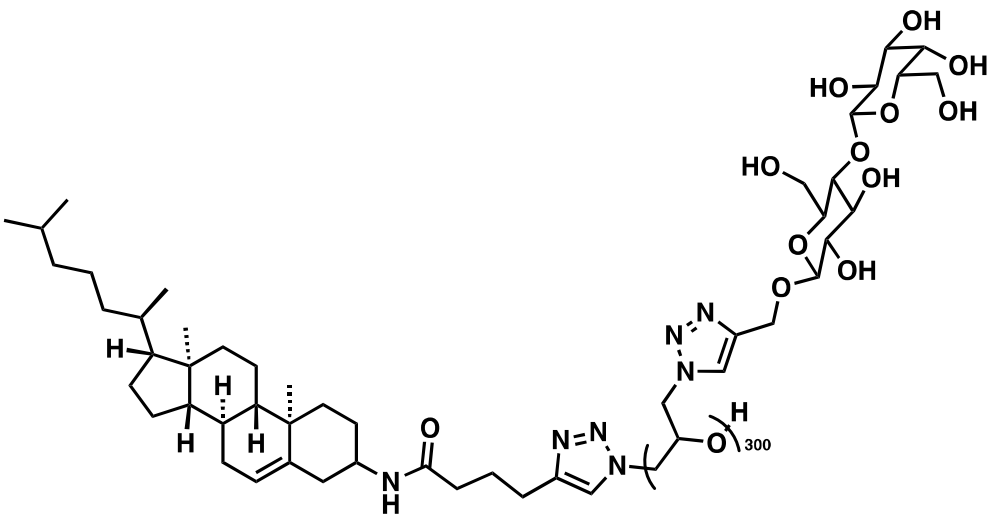

Chol GP

Figure A29: Structure of cholesterol-hexynoic acid linker functionalized lactosyl glycopolymer **Chol GP**

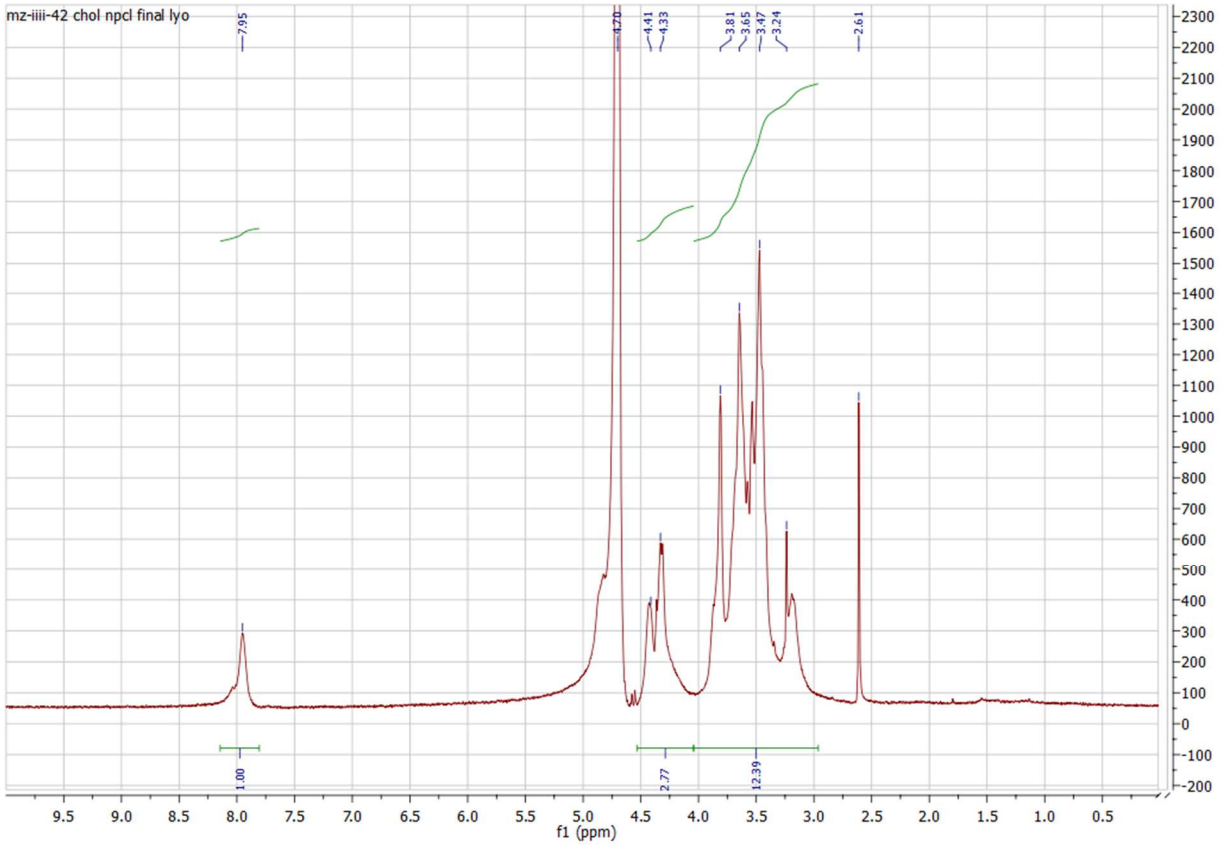

Figure A30: 1H-NMR of cholesterol-hexynoic acid linker functionalized lactosyl glycopolymer **Chol GP**

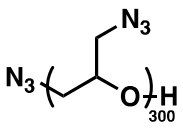

No Endgroup P2

Figure A31: Structure of poly(glycidyl azide) **No Endgroup P2**

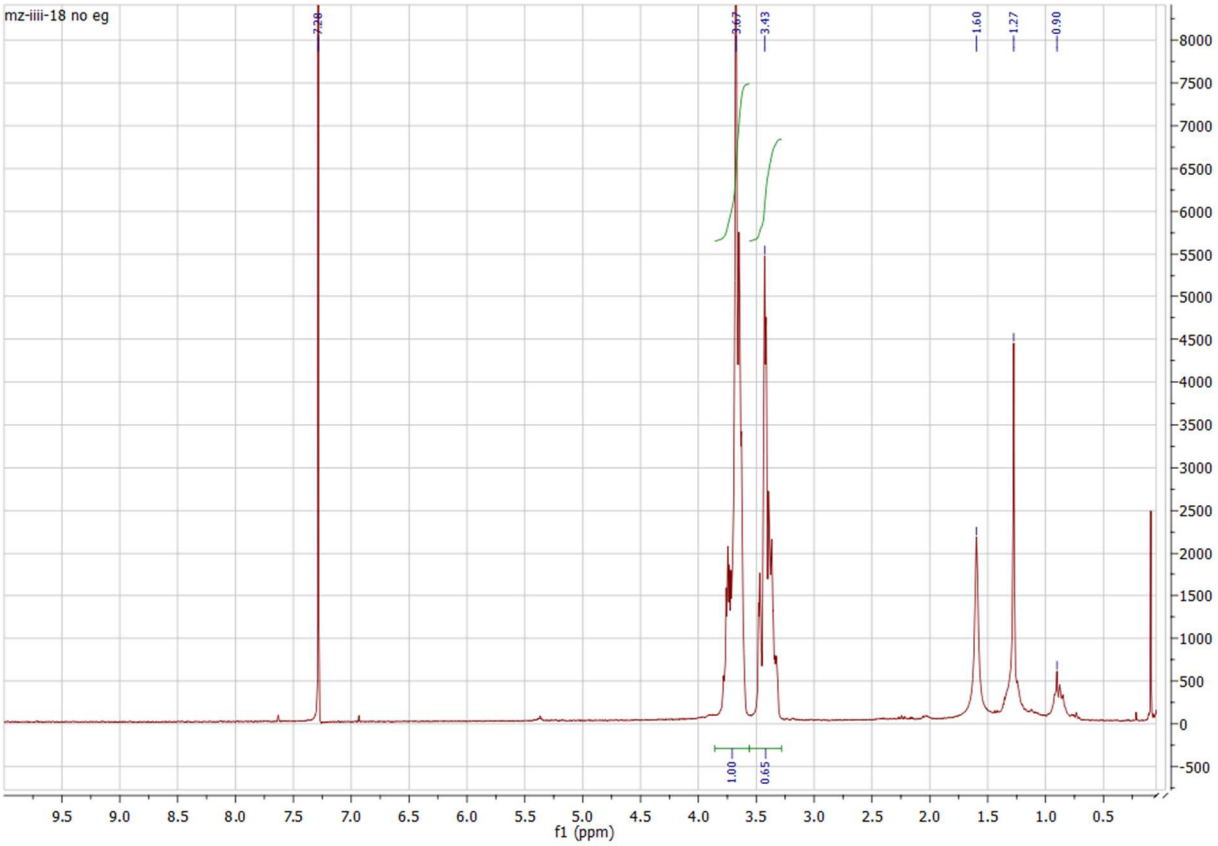

Figure A32: 1H-NMR of poly(glycidyl azide) **No Endgroup P2**

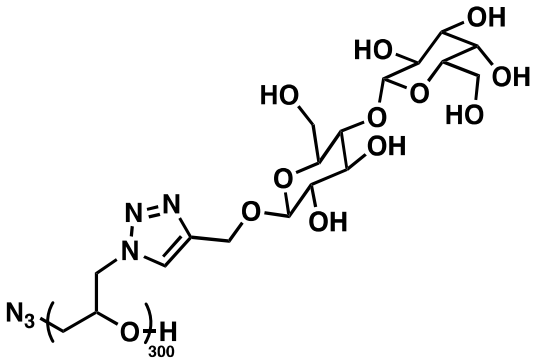

No Endgroup GP

Figure A33: Structure of lactosyl glycpolymer **No Endgroup GP**

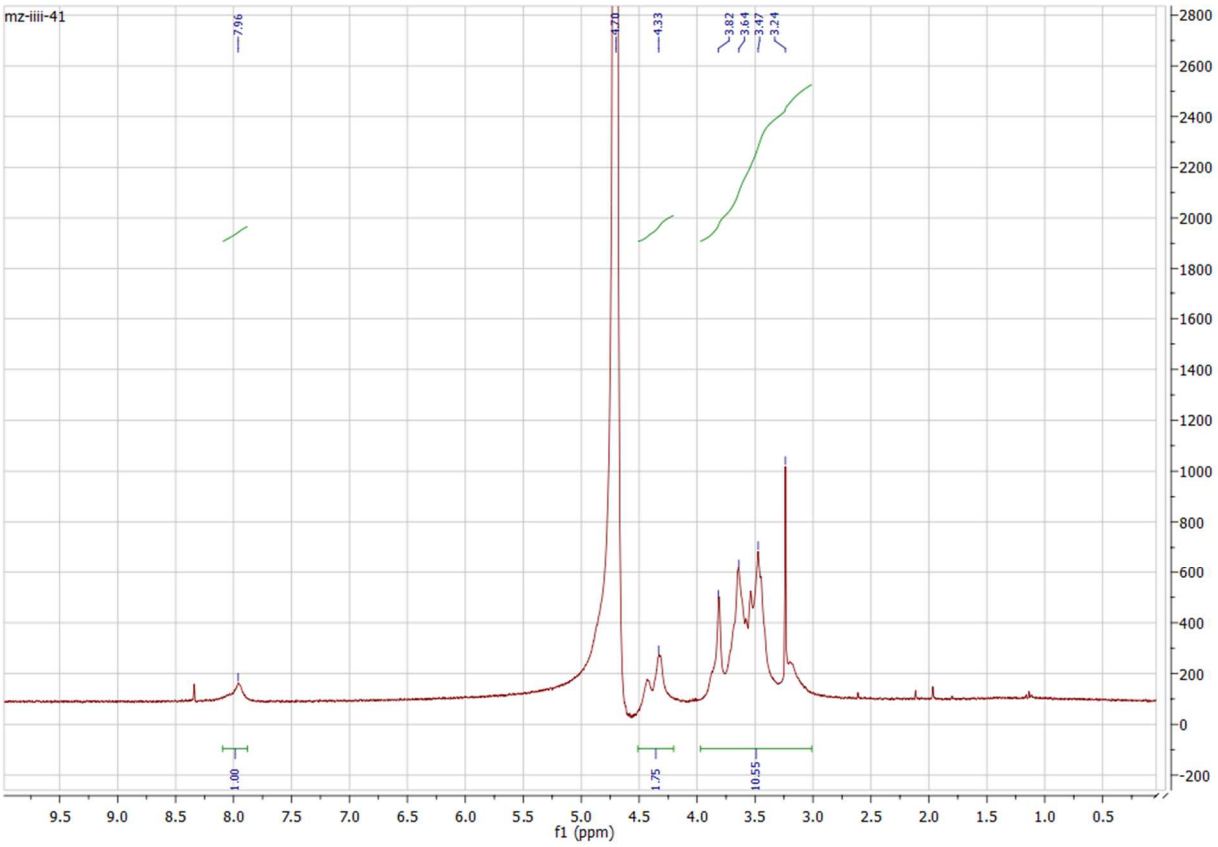

Figure A34: 1H-NMR of lactosyl glycopolymer **No Endgroup GP**

REFERENCES

Chen F, Ricken J, Xu D, Wegner SV. Bacterial Photolithography: Patterning Escherichia coli Biofilms with High Spatial Control Using Photocleavable Adhesion Molecules. *Adv Biosyst*. 2019;3(3):e1800269. doi:10.1002/adbi.201800269

Dube DH, Bertozzi CR. Metabolic oligosaccharide engineering as a tool for glycobiology. Curr. Opin. Chem. Biol. 2003; 7, 616–625. doi:10.1016/j.cbpa.2003.08.006

Esko JD, Stanley P. 2009 Glycosylation mutants of cultured cells. In Essentials of glycobiology (eds A Varki, R Cummings, J Esko et al.), chapter 46, 2nd edn. Cold Spring Harbor, NY: Cold Spring Harbor Laboratory Press.

Ganguly K, Rauth S, Marimuthu S, Kumar S, Batra SK. Unraveling mucin domains in cancer and metastasis: when protectors become predators. *Cancer Metastasis Rev*. 2020;39(3):647-659. doi:10.1007/s10555-020-09896-5

Gaur P, Kucherak OA, Ermakova YG, Shvadchak VV, Yushchenko DA. Nitrobenzyl-based fluorescent photocages for spatial and temporal control of signalling lipids in cells. *Chem Commun (Camb)*. 2019;55(82):12288-12291. doi:10.1039/c9cc05602e

Gervais M, Labbé A, Carlotti S, Deffieux, A. Direct Synthesis of α-Azido,ω-hydroxypolyethers by Monomer-Activated Anionic Polymerization. *Macromolecules*. 2009; 42(7):2395–2400. doi: 10.1021/ma802063s

Govan JM, Uprety R, Thomas M, Lusic H, Lively MO, Deiters A. Cellular delivery and photochemical activation of antisense agents through a nucleobase caging strategy. *ACS Chem Biol*. 2013;8(10):2272-2282. doi:10.1021/cb400293e

Hart GW, Copeland RJ. Glycomics hits the big time. *Cell*. 2010;143(5):672-676. doi:10.1016/j.cell.2010.11.008

Honigfort DJ, Zhang MH, Verespy S, Godula K. Engineering of spectator glycocalyx structures to evaluate molecular interactions at crowded cellular boundaries. *Faraday Discuss.* 2019;219: 138–153. doi: 10.1039/c9fd00024k

Huang ML, Smith RA, Trieger GW, Godula K. Glycocalyx remodeling with proteoglycan mimetics promotes neural specification in embryonic stem cells. *J Am Chem Soc*. 2014;136(30):10565-10568. doi:10.1021/ja505012a

Huang ML, Godula K. Nanoscale materials for probing the biological functions of the glycocalyx. *Glycobiology.* 2016;26(8):797-803. doi: 10.1093/glycob/cww022.

Isabettini S, Liebi M, Kohlbrecher J, Ishikawa T, Fischer P, Windhab EJ, Walde P, Kuster S. Mastering the magnetic susceptibility of magnetically responsive bicelles with 3ß-amino-5-cholestene and complexed lanthanide ions. *Phys Chem Chem Phys*. 2017;19(17):10820-10824. doi:10.1039/c7cp01025g

Kaneko S, Nakayama H, Yoshino Y, Fushimi D, Yamaguchi K, Horiike Y, Nakanishi J. Photocontrol of cell adhesion on amino-bearing surfaces by reversible conjugation of poly(ethylene glycol) via a photocleavable linker. *Phys Chem Chem Phys*. 2011;13(9):4051-4059. doi:10.1039/c0cp02013c

Lindén SK, Sheng YH, Every AL, Miles KM, Skoog EC, Florin TH, Sutton P, McGuckin MA. MUC1 limits Helicobacter pylori infection both by steric hindrance and by acting as a releasable decoy. *PLoS Pathog*. 2009;5(10):e1000617. doi:10.1371/journal.ppat.1000617

Lopez Aguilar A, Briard JG, Yang L, Ovryn B, Macauley MS, Wu P. Tools for studying glycans: recent advances in chemoenzymatic glycan labeling. ACS Chem. Biol. 2017; 12, 611–621. doi:10.1021/acschembio.6b01089

Manabe Y, Kasahara S, Takakura Y, Yang X, Takamatsu S, Kamada Y, Miyoshi E, Yoshidome D, Fukase K. Development of α1,6-fucosyltransferase inhibitors through the diversity-oriented syntheses of GDP-fucose mimics using the coupling between alkyne and sulfonyl azide. Bioorg Med Chem. 2017 Jun 1;25(11):2844-2850. doi: 10.1016/j.bmc.2017.02.036. Epub 2017 Feb 28. PMID: 28284868.

Mauris J, Mantelli F, Woodward AM, Cao Z, Bertozzi CR, Panjwani N, Godula K, Argüeso P. Modulation of ocular surface glycocalyx barrier function by a galectin-3 N-terminal deletion mutant and membrane-anchored synthetic glycopolymers. *PLoS One*. 2013;8(8):e72304. Published 2013 Aug 19. doi:10.1371/journal.pone.0072304

Möckl L. The Emerging Role of the Mammalian Glycocalyx in Functional Membrane Organization and Immune System Regulation. *Front Cell Dev Biol*. 2020;8:253. doi:10.3389/fcell.2020.00253

Nath S, Mukherjee P. MUC1: a multifaceted oncoprotein with a key role in cancer progression. *Trends Mol Med*. 2014;20(6):332-342. doi:10.1016/j.molmed.2014.02.007

Nicolas J, Magli S, Rabbachin L, Sampaolesi S, Nicotra F, Russo L. 3D Extracellular Matrix Mimics: Fundamental Concepts and Role of Materials Chemistry to Influence Stem Cell Fate. *Biomacromolecules*. 2020;21(6):1968-1994. doi:10.1021/acs.biomac.0c00045

Paszek MJ, DuFort CC, Rossier O, Bainer R, Mouw JK, Godula K, Hudak JE, Lakins JN, Wijekoon AC, Cassereau L, Rubashkin MG, Magbanua MJ, Thorn KS, Davidson MW, Rugo HS, Park JW, Hammer DA, Giannone G, Bertozzi CR, Weaver VM. The cancer glycocalyx mechanically primes integrin-mediated growth and survival. *Nature*. 2014;511(7509):319-325. doi:10.1038/nature13535

Purcell SC, Godula K. Synthetic glycoscapes: addressing the structural and functional complexity of the glycocalyx. *Interface Focus.* 2019; 9: 20180080. doi.org/10.1098/rsfs.2018.0080

Stanley P. Chinese hamster ovary cell mutants with multiple glycosylation defects for production of glycoproteins with minimal carbohydrate heterogeneity. *Mol Cell Biol*. 1989;9(2):377-383. doi:10.1128/mcb.9.2.377

Stanley P, Taniguchi N, Aebi M. N-Glycans. 2017. In: Varki A, Cummings RD, Esko JD, et al., editors. Essentials of Glycobiology [Internet]. 3rd edition. Cold Spring Harbor (NY): Cold Spring Harbor Laboratory Press; 2015-2017. Chapter 9.

Varki A, Gagneux P. Biological Functions of Glycans. 2017. In: Varki A, Cummings RD, Esko JD, et al., editors. Essentials of Glycobiology [Internet]. 3rd edition. Cold Spring Harbor (NY): Cold Spring Harbor Laboratory Press; 2015-2017. Chapter 7.

Wegner SV, Sentürk OI, Spatz JP. Photocleavable linker for the patterning of bioactive molecules. *Sci Rep*. 2015;5:18309. Published 2015 Dec 16. doi:10.1038/srep18309